

# Geochemistry, Geophysics, Geosystems®

## RESEARCH ARTICLE

10.1029/2022GC010474

### Key Points:

- Deciphering the fossil-to-active hydrothermal system on Zannone Island in which magmatic and meteoric fluids mixed
- Polyphase and long-lived hydrothermal activity associated with mantle- and crustal-derived magmas
- Fluid mixing and fluid-rock interaction led to fluid neutralization, cooling, embrittlements, alteration, and minor ore minerals

### Supporting Information:

Supporting Information may be found in the online version of this article.

### Correspondence to:

M. Curzi,  
manuel.curzi@unibo.it

### Citation:

Curzi, M., Caracausi, A., Rossetti, F., Rabiee, A., Billi, A., Carminati, E., et al. (2022). From fossil to active hydrothermal outflow in the back-arc of the central Apennines (Zannone Island, Italy). *Geochemistry, Geophysics, Geosystems*, 23, e2022GC010474. <https://doi.org/10.1029/2022GC010474>

Received 8 APR 2022

Accepted 21 SEP 2022

### Author Contributions:

**Conceptualization:** M. Curzi, A. Caracausi, F. Rossetti, A. Billi, E. Carminati

**Data curation:** M. Curzi, A. Caracausi, F. Rossetti, A. Billi, E. Carminati, L. Aldega, S. M. Bernasconi, C. Boschi, K. Drivenes, A. L. Rizzo, B. E. Sørensen

**Formal analysis:** M. Curzi, A. Caracausi, F. Rossetti, A. Billi, E. Carminati, S. M. Bernasconi, K. Drivenes, A. L. Rizzo, B. E. Sørensen







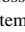

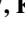



**Funding acquisition:** M. Curzi, E. Carminati

**Investigation:** M. Curzi, F. Rossetti, A. Rabiee, A. Billi, E. Carminati, L. Aldega

© 2022. The Authors.

This is an open access article under the terms of the [Creative Commons Attribution License](#), which permits use, distribution and reproduction in any medium, provided the original work is properly cited.

## From Fossil to Active Hydrothermal Outflow in the Back-Arc of the Central Apennines (Zannone Island, Italy)

M. Curzi<sup>1,2</sup> , A. Caracausi<sup>3</sup> , F. Rossetti<sup>4</sup> , A. Rabiee<sup>4</sup> , A. Billi<sup>5</sup> , E. Carminati<sup>1</sup> , L. Aldega<sup>1</sup> , S. M. Bernasconi<sup>6</sup> , C. Boschi<sup>7</sup> , K. Drivenes<sup>8</sup> , A. L. Rizzo<sup>3,9</sup> , and B. E. Sørensen<sup>8</sup> 

<sup>1</sup>Dipartimento di Scienze della Terra, Sapienza Università di Roma, Roma, Italy, <sup>2</sup>Dipartimento di Scienze Biologiche, Geologiche ed Ambientali – BiGeA, Università degli studi di Bologna, Bologna, Italy, <sup>3</sup>Istituto Nazionale di Geofisica e Vulcanologia, Sezione di Palermo, Palermo, Italy, <sup>4</sup>Dipartimento di Scienze, Università Roma Tre, Rome, Italy, <sup>5</sup>Consiglio Nazionale delle Ricerche, IGAG, Rome, Italy, <sup>6</sup>Geological Institute, ETH Zürich, Zürich, Switzerland, <sup>7</sup>Istituto di Geoscienze e Georisorse, Consiglio Nazionale delle Ricerche, Pisa, Italy, <sup>8</sup>Department of Geoscience and Petroleum, Norwegian University of Science and Technology, Trondheim, Norway, <sup>9</sup>Istituto Nazionale di Geofisica e Vulcanologia, Sezione di Milano, Milano, Italy

**Abstract** Post-orogenic back-arc magmatism is accompanied by hydrothermal ore deposits and mineralizations derived from mantle and crustal sources. We investigate Zannone Island (ZI), back-arc Tyrrhenian basin, Italy, to define the source(s) of mineralizing hydrothermal fluids and their relationships with the regional petrological-tectonic setting. On ZI, early Miocene thrusting was overprinted by late Miocene post-orogenic extension and related hydrothermal alteration. Since active submarine hydrothermal outflow is reported close to the island, Zannone provides an ideal site to determine the *P-T-X* evolution of the long-lived hydrothermal system. We combined field work with microstructural analyses on syn-tectonic quartz veins and carbonate mineralizations, X-ray diffraction analysis, microthermometry and element mapping of fluid inclusions (FIs), C, O, and clumped isotopes, and analyses of noble gases (He-Ne-Ar) and CO<sub>2</sub> content in FIs. Our results document the evolution of a fluid system of magmatic origin with increasing mixing of meteoric fluids. Magmatic fluids were responsible for quartz veins precipitation at ~125 to 150 MPa and ~300°C–350°C. With the onset of extensional faulting, magmatic fluids progressively interacted with carbonate rocks and mixed with meteoric fluids, leading to (a) host rock alteration with associated carbonate and minor ore mineral precipitation, (b) progressive fluid neutralization, (c) cooling of the hydrothermal system (from ~320°C to ~86°C), and (d) embrittlement and fracturing of the host rocks. Both quartz and carbonate mineralizations show noble gases values lower than those from the adjacent active volcanic areas and submarine hydrothermal systems, indicating that the fossil-to-active hydrothermal history is associated with the emplacement of multiple magmatic intrusions.

## 1. Introduction

Back-arc basins are often characterized by diffuse crustal- and mantle-derived magmatism, alteration and ore deposits associated with hydrothermal outflow (e.g., Fouquet et al., 1991; Li et al., 2020; Peccerillo, 2005; Wolfram et al., 2019). Active back-arc mineralizing hydrothermal systems (e.g., Halbach et al. (1989) and Yeats et al. (2017) for the Okinawa trough; e.g., Marani et al. (1997) for the Tyrrhenian basin), are considered a geodynamic environment that can generate massive volcanogenic sulfide ore deposits (Kuroko-type; Ohmoto, 1996). The properties and compositions of such sulfide ore deposits are related to their degree of structural development (Fouquet et al., 1993). Mature back-arc systems, such as the Lau (Fouquet et al., 1991) and North Fiji basins (Bendel et al., 1993), floored by basaltic crust, are characterized by hydrothermal deposits similar to mid-ocean ridge and Cyprus type sulfide deposits. In nascent back-arcs, such as the Okinawa trough (Halbach et al., 1989), considered as the present-day environments for Kuroko-type mineralization (Ohmoto, 1996), the composition of the hydrothermal systems is controlled by extensional tectonics in continental crust and by associated bimodal volcanism. Some studies have appreciated the role of faulting in the development of back-arc ore deposits (e.g., Binns and Scott (1993) for the Manus Basin; Ishibashi et al. (2015) and Yeats et al. (2017) for the Okinawa trough), but detailed information on the relationship between faulting and fluid circulation are scarce.

The Neogene-Quaternary Tyrrhenian back-arc region of the Apennine belt represents a key area to investigate fluid-rock interaction, rock alteration and ore-forming processes associated with structurally controlled hydrothermal outflow during post-orogenic magmatism (Brogi et al., 2020; Dini, 2003; Dini et al., 2008; Fulignati, 2018;

**Methodology:** M. Curzi, A. Caracausi, F. Rossetti, A. Billi, L. Aldega, S. M. Bernasconi, C. Boschi, K. Drivenes, A. L. Rizzo, B. E. Sørensen

**Project Administration:** F. Rossetti, A. Billi, E. Carminati

**Resources:** A. Caracausi, S. M. Bernasconi, C. Boschi

**Software:** M. Curzi, L. Aldega, S. M. Bernasconi, C. Boschi, K. Drivenes, A. L. Rizzo, B. E. Sørensen

**Supervision:** M. Curzi, A. Caracausi, F. Rossetti, A. Billi, E. Carminati, L. Aldega, C. Boschi

**Validation:** M. Curzi, A. Caracausi, F. Rossetti, A. Rabiee, E. Carminati, L. Aldega, S. M. Bernasconi, C. Boschi, K. Drivenes, A. L. Rizzo, B. E. Sørensen

**Visualization:** M. Curzi

**Writing – original draft:** M. Curzi, A. Caracausi, F. Rossetti, A. Rabiee, A. Billi, E. Carminati, L. Aldega, S. M. Bernasconi, C. Boschi, K. Drivenes, A. L. Rizzo, B. E. Sørensen

**Writing – review & editing:** M. Curzi, A. Caracausi, F. Rossetti, A. Rabiee, A. Billi, E. Carminati, L. Aldega, S. M. Bernasconi, C. Boschi, K. Drivenes, A. L. Rizzo, B. E. Sørensen

Minissale et al., 1997, 2000; Paoli et al., 2019; Rossetti et al., 2011; Serri et al., 1993; Vignaroli et al., 2016). Several examples of fossil and active structurally controlled sulfide hydrothermal deposits are documented in the inner sector of the Apennines chain (Tuscan Archipelago and Colline Metallifere of the Tuscan region), where diffuse polymetallic sulphide ores are reported and exploited since historical times (Brogi & Fulignati, 2012; Brogi et al., 2011; Corsini et al., 1980; Cortecci et al., 1985; Dini et al., 2008; Liotta et al., 2010; Martarelli et al., 1995; Rossetti et al., 2011; Figure 1a). Understanding the processes leading to hydrothermal flow and the tectonic control on the circulation of mineralizing fluids in this tectonic realm is therefore essential to elucidate the ore potential of the Tyrrhenian back-arc extension.

The geology of Zannone Island (ZI; Figure 1) has recently been reevaluated and interpreted as a remnant of the southern, offshore continuation of the Tuscan Domain, where early Miocene thrusting and post-orogenic late Messinian-early Pliocene extensional tectonics have been documented (Curzi et al., 2020). Similarly to the Tuscan region, the post-orogenic evolution on ZI was accompanied by volcanism and submarine hydrothermal activity and degassing is still active (Curzi et al., 2020; Ingrassia et al., 2015; Italiano et al., 2019; Martorelli et al., 2016), confirming the pioneering investigation of Tricoli (1855) who recognized the presence of sulfur-rich springs in the offshore of ZI. In detail, on the shelf of ZI, shallow water depressions at about 150 m depth, including the Zannone Giant Pockmark (ZGP), host active hydrothermal vents (Conte, Perinelli, et al., 2020; Ingrassia et al., 2015). Assessing the tectonic control and geochemical fingerprints of fossil hydrothermal fluid flow in ZI can contribute to trace the long term and structurally controlled hydrothermal activity in the area and to refine our understanding of the modes, source and styles of active degassing in the Tyrrhenian back-arc domain of the Apennines.

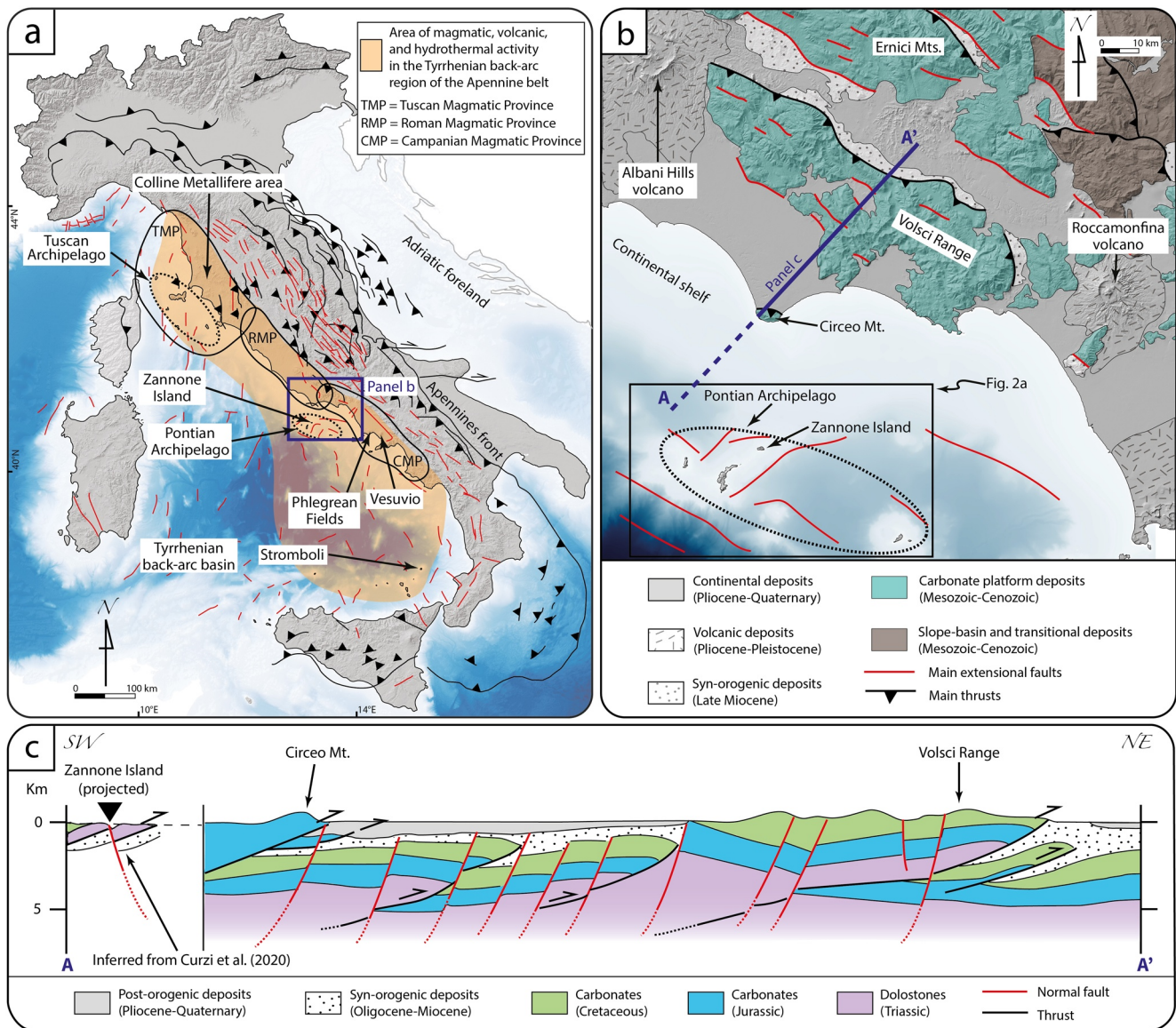
In this paper, we characterize the structural control exerted by post-orogenic tectonics in ZI on the hydrothermal fluid infiltration and mineralization by focusing on syn-tectonic quartz veins reworked by carbonate mineralizations. We integrate meso- to micro-scale structural investigations with petrographic analyses, microthermometry and element mapping of fluid inclusions (FIs), C, O stable and clumped isotopes, noble gases (He, Ne, and Ar) systematics, and CO<sub>2</sub> measurements to define the source of the hydrothermal fluids. We show that syn-tectonic fluids at ZI mark the transition from magmatic to meteoric fluids in a cooling deformation regime.

## 2. Geological Setting

### 2.1. Central Apennines

The central Apennine belt is an E-NE-verging, late Oligocene to Present fold-and-thrust belt (Figure 1) that resulted from the W-directed subduction of the Adriatic continental lithosphere below the European continental margin (Carminati et al., 2010; Faccenna et al., 2001; Malinverno & Ryan, 1986). Subduction and westward underthrusting of the Adriatic lithosphere progressively widened the orogenic Apennine wedge, leading to the migration of the foredeep-foreland system toward the east (Cavinato & Celles, 1999; Patacca & Scandone, 2007; Cosentino et al., 2010; Carminati et al., 2010; Figure 1).

Orogenic accretion in the central Apennines began in late Oligocene-Miocene time and was accommodated in a foreland wedge-top sequence by NE-verging thrusts, which piled up pre- and syn-orogenic sedimentary deposits of the Adriatic plate (Cosentino et al., 2010; Curzi et al., 2020; Patacca et al., 1990; Figure 1). The pre-orogenic deposits consist of Late Triassic-Middle Miocene carbonates deposited in shallow and deep-water environments (e.g., Cosentino et al., 2010; Figure 1). The syn-orogenic deposits consist of Oligocene-Miocene siliciclastic sandstones, marls and clays deposited in foredeep and wedge-top basins (Billi & Tiberti, 2009; Cosentino et al., 2010; Curzi et al., 2020; Merlini & Mostardini, 1986; Patacca et al., 1990; Figure 1). The eastward migration of the Apennine belt was accompanied by the Tyrrhenian back-arc opening and associated crustal thinning, as a result of lithosphere rollback. This process led to the progressive eastward migration of crustal stretching toward the axial (eastern) sector of the Apennine belt, associated with vigorous magmatic activity (Carminati et al., 2010; Faccenna et al., 2001; Jolivet et al., 1998; Malinverno & Ryan, 1986; Figure 1). The magmatism, which gave rise to the Tuscan, Roman and Campanian Magmatic Provinces (Figure 1a) was accompanied by locally still active hydrothermal activity and degassing of deep sourced fluids (Caracausi et al., 2015; Caracausi & Paternoster, 2015; Italiano et al., 2019; Vignaroli et al., 2015; Figure 1a), in particular within the Tyrrhenian (western) side of the Apennine belt (Acocella & Funicello, 2006; Brogi, 2004; Caracausi et al., 2013; Chiodini et al., 2010; Dekov & Savelli, 2004; Italiano et al., 2014; Minissale et al., 1997; Vignaroli et al., 2015).



**Figure 1.** (a) Simplified structural map of Italy showing the main thrusts and extensional faults. The area of post-compressive magmatic, volcanic, and hydrothermal activity in the Tyrrhenian back-arc region of the central-northern Apennines is shown. (b) Simplified geological map of the inner central Apennines. (c) Schematic geological cross section showing the first order structure of the inner Apennine belt. The geology of Zannone Island is projected and inferred from Curzi et al. (2020). The trace of the schematic geological cross section is shown in panel (b).

## 2.2. Pontian Archipelago and Zannone Island

ZI is part of the Pontian Archipelago, which is located in the Tyrrhenian back-arc basin on the western margin of the central Italian continental shelf (Figure 1). Tavani et al. (2021) include the Pontian Archipelago in the Ponza-Alife accommodation zone, which is interpreted as a pristine deep-seated transform fault system located in the subducting plate and was inherited from an Early Jurassic rifting episode, which caused the lateral juxtaposition of different rift domains.

In the Pontian Archipelago, submarine hydrothermal vents actively emit  $\text{CO}_2$ -dominated fluids with a mantle-derived geochemical component, sourced from cooling magmatic bodies (Martorelli et al., 2016; Ingrassia et al., 2015; Italiano et al., 2019; Figures 2a and 2b). The isotopic signatures in gas and water emitted from these sea bottom manifestations are up to  $3.7 \text{ Ra} \pm 0.1$  (Figure 9a; Martorelli et al., 2016; Italiano et al., 2019). These values are in the range of those measured in fluids from the closest peri-Tyrrhenian volcanic systems and in FIs



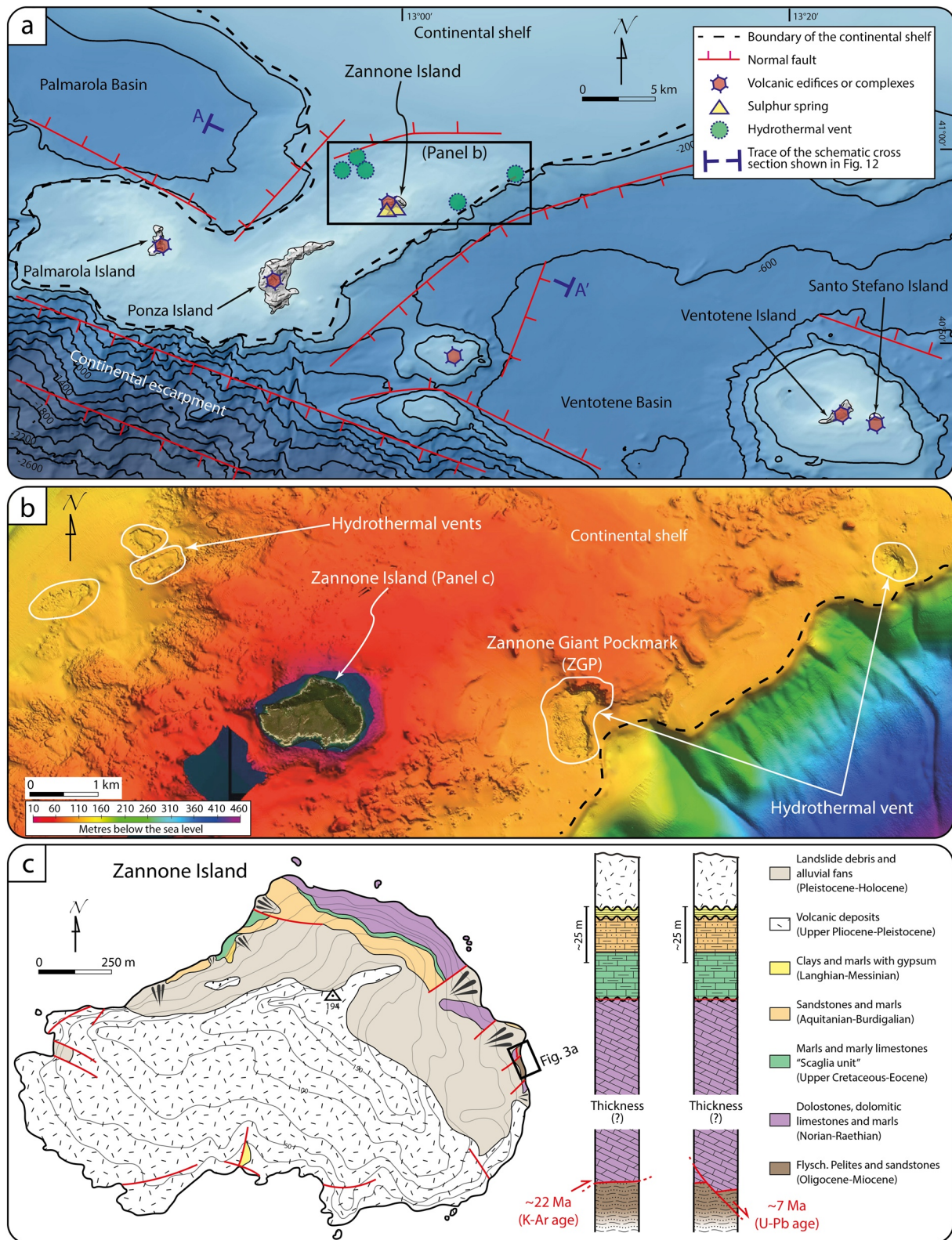


Figure 2.



of minerals from the nearby volcanic complexes (2.5Ra, Roccamonfina, Phlegrean Fields, and Vesuvius < He isotopic signature <5.2Ra, Ischia and Procida; Martelli et al., 2004; Figure 1a). The Pontian Archipelago is located at the boundary between the Tuscan and Roman Magmatic Provinces (Figure 1a) and is constituted by five islands generally subdivided into two main groups based on their structural and volcanic characteristics (Chiocci & Orlando, 1996; Pantosti & Velonà, 1986). The eastern group is composed of Ventotene and Santo Stefano Islands, representing the subaerial portion of a large, submerged stratovolcano with ages of 0.8–0.13 Ma (Metrich et al., 1988; Pantosti & Velonà, 1986; Peccerillo, 2005; Figure 2a). The western group includes the Island of Ponza, Palmarola, and Zannone and is located on a structural high separating the Plio-Quaternary Palmarola (to the NW) and Ventotene (to the SE) Basins (Cadoux et al., 2005; De Rita et al., 1986; Peccerillo, 2005; Zitellini et al., 1984; Figure 2a). The sector with structural high is bounded by NE-SW- and NW-SE-striking faults related to the early Pliocene extension of the Tyrrhenian back-arc basin (Curzi et al., 2020; De Rita et al., 1986; Martorelli et al., 2016; Pantosti & Velonà, 1986; Zitellini et al., 1984; Figure 2a). The western Pontian Islands are constituted mostly by trachytes and rhyolites, with ages ranging from 4.2 to 1 Ma (Cadoux et al., 2005; Peccerillo, 2005). These volcanic rocks, originally interpreted as part of the dominantly crustal anatectic Tuscan Magmatic Province (Turi et al., 1991; Figure 1a), were recently interpreted as products of mantle-derived magmas associated with the Roman Magmatic Province (Conte, Perinelli, et al., 2020; Figure 1a). These volcanics cover a Mesozoic-Cenozoic sedimentary substratum exposed solely along the eastern coast of ZI. From bottom to top, the substratum consists of Oligocene-Miocene turbidites (i.e., flysch) which were overthrust by Triassic dolostone at ~22 Ma, and was later affected by normal faults at ~7 Ma (Curzi et al., 2020; Segre, 1954; Figure 2c). The Triassic dolostone are overlain by Upper Cretaceous-Eocene pelagic marls and marly limestones, followed by Aquitanian-Burdigalian sandstones and marls and Langhian-Messinian clays and marls with gypsum (De Rita et al., 1986; Parotto & Pratlurion, 1975; Figure 2c). Occurrence of gypsum within the Langhian-Messinian clays and marls was interpreted as the result of circulation of hydrothermal fluids with volcanic origin (De Rita et al., 1986).

### 3. Methods

The paleo-hydrothermal fluid flow in ZI was characterized with a multidisciplinary approach that integrates field and geochemical analyses aimed to constrain the pressure-temperature-composition (*P-T-X*) of the infiltrating fluid(s). Field work was aimed at defining the control on fluid flow exerted by structural (secondary) permeability and to collect representative samples. Laboratory analyses include (a) microtextural investigations through optical microscopy and scanning electron microscopy on veins, alteration selvages, and host rocks; (b) XRD analyses of host rocks, (c) microthermometry coupled with elemental mapping (EDS maps) of FIs in quartz and carbonate mineralizations; (d) stable O and C systematics and clumped isotopes (mineralization and host rock); and (e) noble gas (He, Ne, and Ar), H<sub>2</sub>O, and CO<sub>2</sub> systematics of the mineralizing fluid(s). The analytical methods and protocols are fully described in Methods in Supporting Information S1.

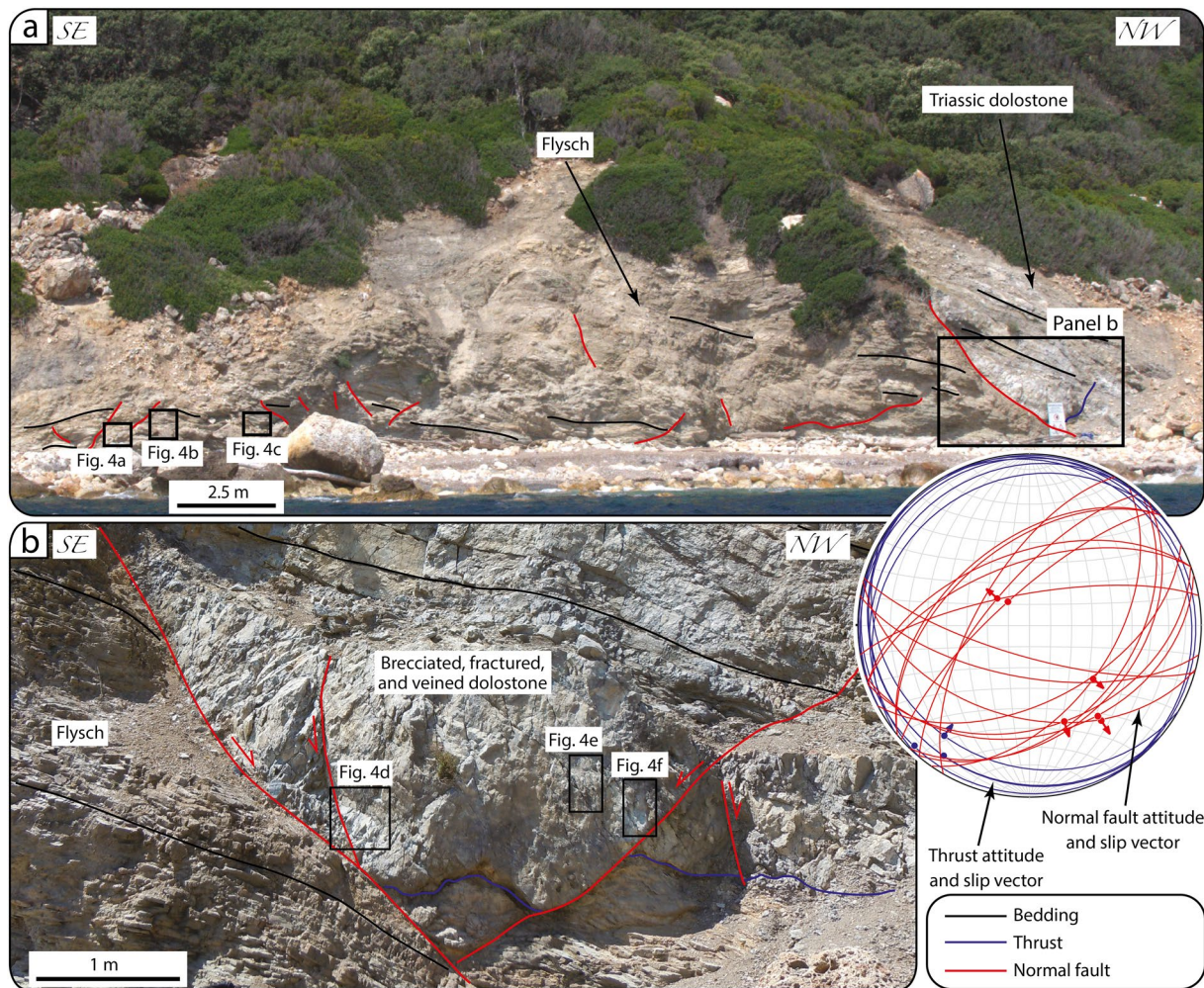
## 4. Results

### 4.1. Field Observations

Field work was focused on a ~100 m long outcrop along the eastern coast of the ZI (Figures 2b and 3a). A major low-angle thrust is exposed controlling the contact between Triassic dolostones in the fault hanging wall and Oligocene-Miocene siliciclastic rocks in the fault footwall, respectively. The thrust is cut and displaced by high-angle, NE-SW striking normal faults (Curzi et al., 2020; Figures 2, 3a and 3b).

Up to 7 cm thick quartz veins spaced 5–10 cm apart, occur at the footwall of the thrust (i.e., within the siliciclastic rocks) and are organized in two mutually cross-cutting, sub-orthogonal sets. One set shows a sub-horizontal

**Figure 2.** (a) Bathymetric map of the central Italian western margin showing the Pontian Archipelago, Palmarola and Ventotene Basins, main faults, hydrothermal depressions, sulfur springs, and volcanic edifices/volcanic complexes of the area. (Bathymetric map from European Marine Observation and Data Network, EMODnet [www.emodnet.eu](http://www.emodnet.eu); boundary of the continental shelf from Pantosti and Velonà (1986); normal faults from Zitellini et al. (1984) and Martorelli et al. (2016); sulfur springs from Tricoli (1855); hydrothermal depressions from Martorelli et al. (2016) and volcanic edifices or complexes from Cuffaro et al. (2016).) (b) Bathymetric map of the seafloor close to Zannone Island showing the five hydrothermal depressions which include the Zannone Giant Pockmark (ZGP), and which host active hydrothermal vents. (c) Simplified geological map and stratigraphy of Zannone Island showing the sedimentary cover exposed on the island, the structural relationship between the Oligocene-Miocene siliciclastic rocks and the overlying Triassic dolostone, and the location of the studied exposure (modified after Curzi et al., 2020).



**Figure 3.** (a) Panoramic view of the eastern coast of Zannone Island with simplified geological interpretation and studied exposures (see location in Figure 2c). Note the normal faults cutting the entire exposure. (b) Tectonic contacts between the Oligocene-Miocene siliciclastic rocks and the brecciated, fractured and veined Triassic dolostone. Contacts consist of a thrust fault and at least two later opposite-dipping (NW and SE) normal faults. Schmidt net (lower hemisphere projection) shows attitude of thrust and normal faults of panels (a and b) and related kinematic indicators.

attitude (i.e., parallel to the bedding), the other defines a sub-vertical (perpendicular to the bedding) non-systematic array (Figures 4a–4c). Occasionally, millimetric carbonate veins cut and rework the quartz veins (see below).

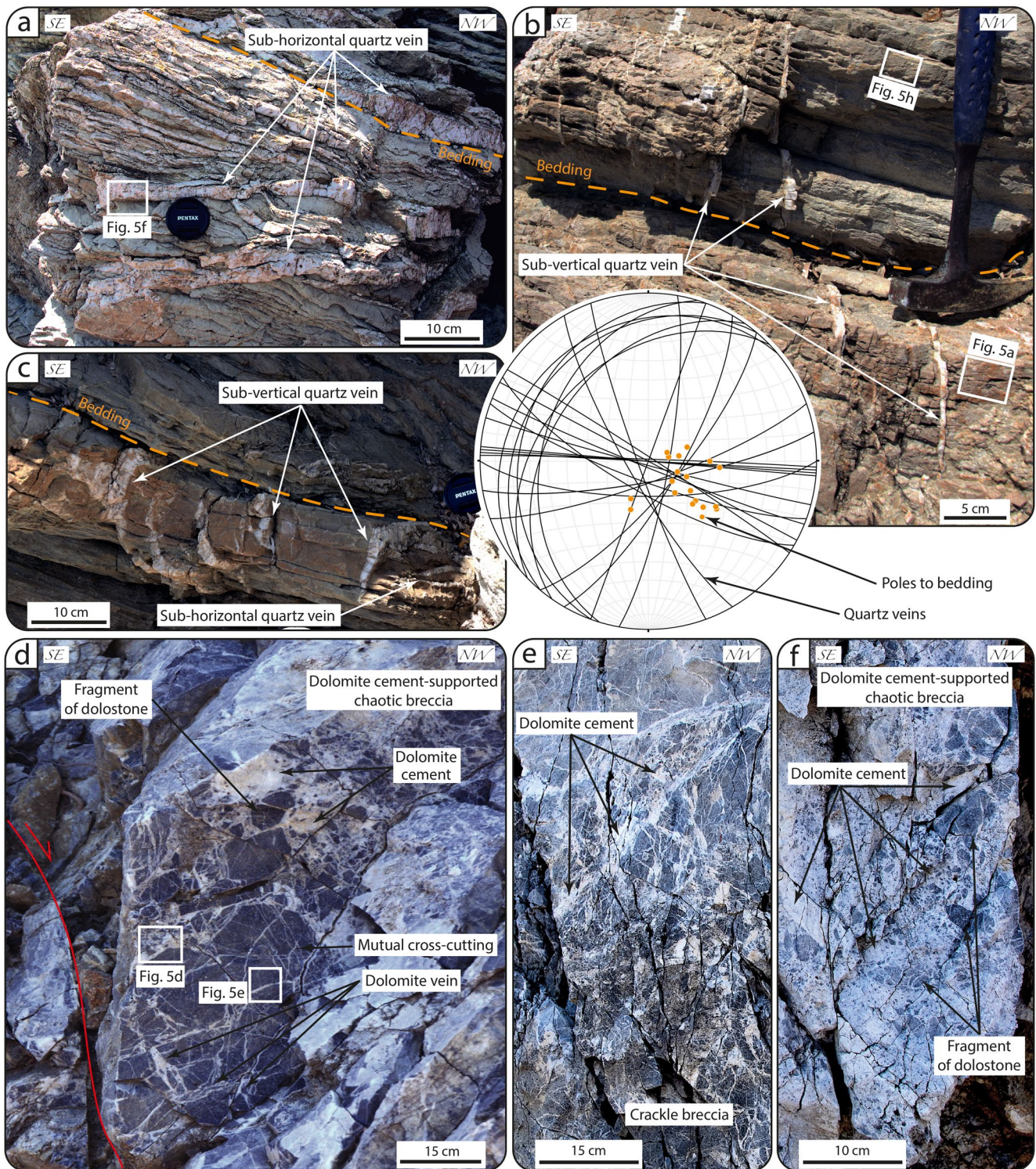
The Triassic dolostones (thrust hanging wall) exhibit fractures, variably oriented veins localized adjacent to the high-angle, and NE-SW striking normal faults that cut across the thrust surface (Figures 3 and 4d–4f). Fault breccias are cemented by carbonate mineralization(s) and are characterized by crackle (Mort & Woodcock, 2008; Figure 4e) and/or cement-supported chaotic fabric (Woodcock et al., 2006; Figure 4f). Variably oriented carbonate veins, up to ~2 cm thick, are observed, with a spacing varying from 1 to 10 cm, and exhibiting mutual cross-cutting relationships (Figure 4d).

## 4.2. Microscale Texture and Mineralogy

### 4.2.1. Host Rocks

The detrital mineral assemblage of the Oligocene-Miocene siliciclastic rocks is composed of up to 90% quartz, subordinate muscovite, chlorite, plagioclase, and opaque minerals, embedded within a carbonate cement with agglomerated or very fine-grained texture (Figure 5a). Small variations in grain size mark the primary foliation (bedding,  $S_0$ ; Figure 5b). A weakly developed secondary foliation ( $S_1$ ) is rarely observed, usually sub-parallel to  $S_0$  (Figure 5c), occasionally associated with fine-grained muscovite bands (up to 50  $\mu\text{m}$  wide, spaced





**Figure 4.** (a) Sub-horizontal quartz veins within the Oligocene-Miocene siliciclastic rocks parallel to the bedding (see location in Figure 3a). (b) Sub-vertical quartz veins within the Oligocene-Miocene siliciclastic rocks sub-perpendicular to the bedding (see location in Figure 3a). (c) Sub-horizontal and sub-vertical quartz veins within the Oligocene-Miocene siliciclastic rocks (see location in Figure 3a). Schmidt net (lower hemisphere) shows poles to bedding and attitude of quartz veins. (d) Dolomite veins and dolomite cement-supported chaotic fault breccia within the Triassic dolostone close to the normal faults which downfault the Triassic dolostone onto the Oligocene-Miocene siliciclastic rocks (see location in Figure 3b). Note the mutual cross-cutting relationship between dolomite veins. (e) Crackle fault breccia with dolomite cement within the Triassic dolostone (see location in Figure 3b). (f) Dolomite-cement-supported chaotic fault breccia within the Triassic dolostone close by the normal faults which downfault the Triassic dolostone onto the Oligocene-Miocene siliciclastic rocks (see location in Figure 3b). Some sampling sites for microscale analyses are also shown.



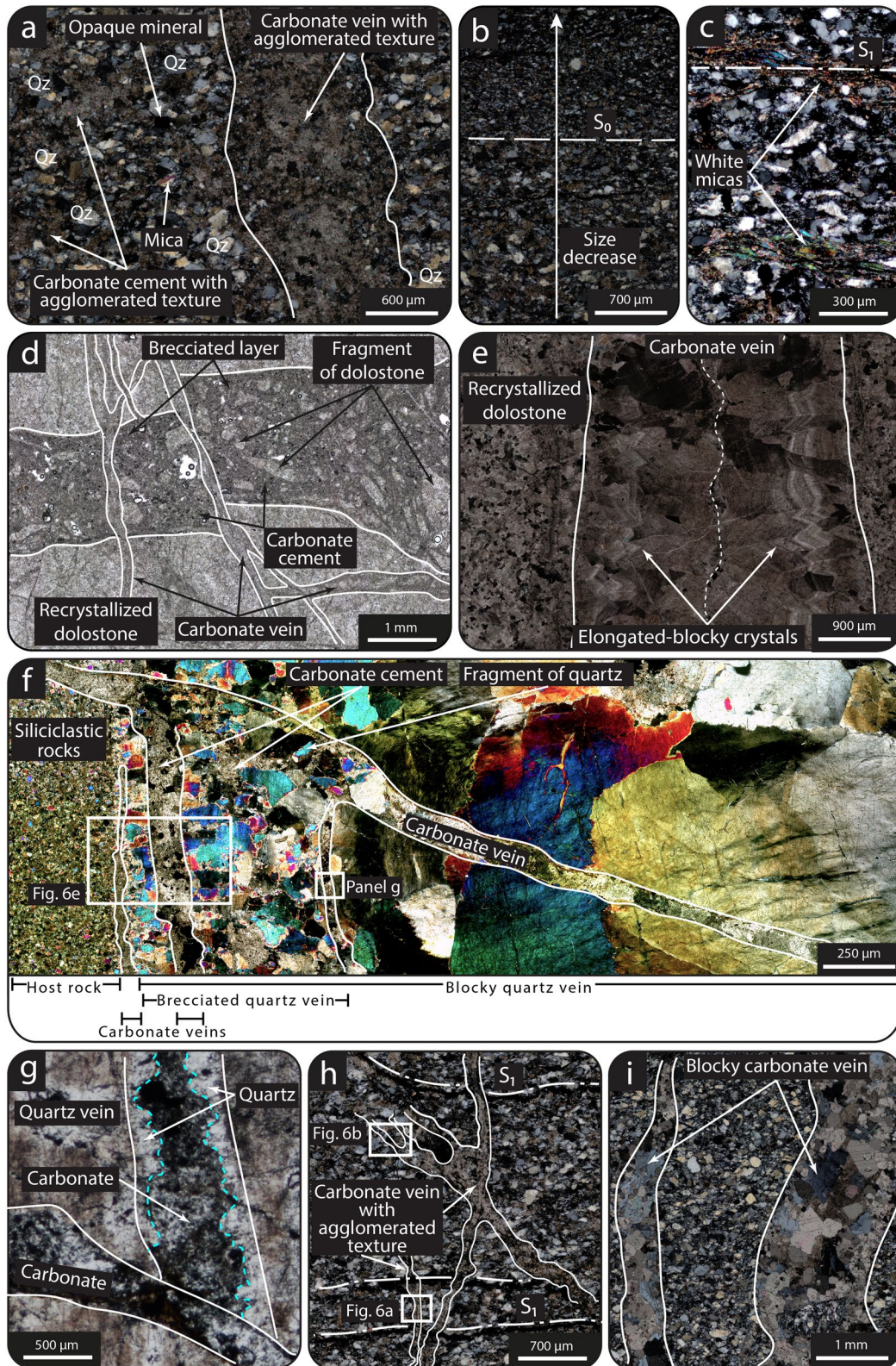


Figure 5.



tens-to-hundreds of  $\mu\text{m}$  apart; Figure 5c). The XRD data in this study expand upon the pre-existing data set published by Curzi et al. (2020), where the mineralogical composition of pelite beds within the siliciclastic rocks was documented. Semi-quantitative XRD analysis of the  $<2\ \mu\text{m}$  grain size fraction of sandstone layers within the siliciclastic rocks (Table S1 in Supporting Information S1) shows an illite-rich composition (47%–68%) with variable amounts of smectite (10%–33%), chlorite (8%–40%), and kaolinite (4%–12%). Non-clay minerals such as quartz occur in the fine fraction as well. The clay fraction of the Triassic dolostones is mostly composed of smectite (from 50% to 97%), with subordinate amounts of chlorite (2%–11%), mixed layers chlorite-smectite (1%–9%), and illite (generally  $<1\%$ ). Quartz and dolomite were also observed.

The Triassic dolostones show evidence of secondary recrystallization which overprints the primary sedimentary features (Figures 5d and 5e). The carbonate cement within brecciated layers shows an agglomerated texture and embeds micrometric to millimetric fragments of dolostones (Figure 5d).

#### 4.2.2. Veins

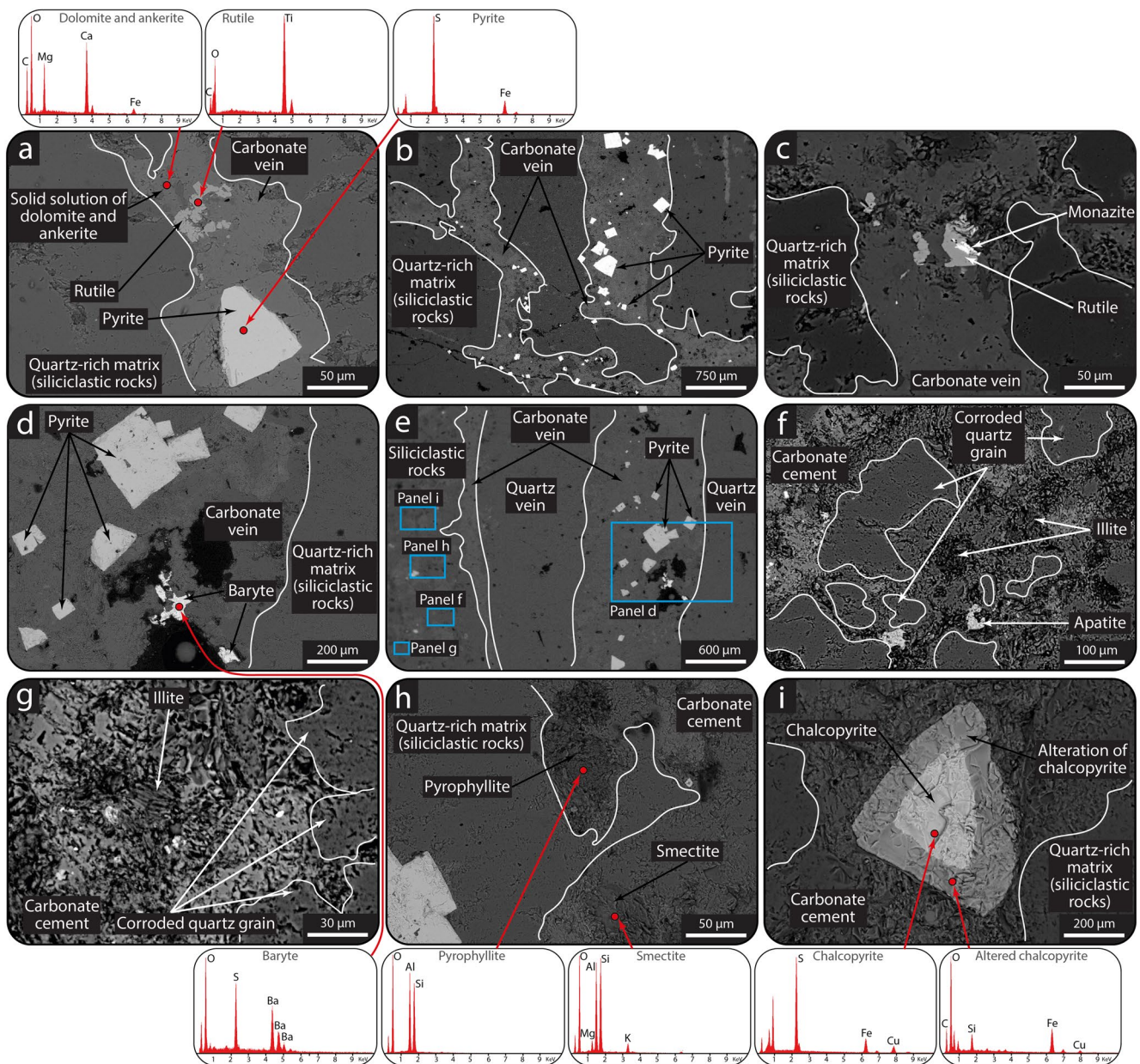
The quartz veins in the siliciclastic rocks (thrust footwall) are devoid of accessory minerals, except for rare pyrite crystals. Quartz has a blocky texture, with up to 2 mm large grains (Figure 5f). Carbonate veins (mm-sized) either cut the quartz veins or rework the quartz vein/host rock contacts (Figure 5f). Carbonate veins show either agglomerated (or very fine-grained) (Figures 5a and 5h) or blocky textures (Figure 5i). Quartz veins are also crushed into fragments embedded within a carbonate cement (Figure 5f). Composite veins are observed and are characterized by early quartz crystals growing from the vein walls toward the center and late carbonates in the center of the vein (Figure 5g). Such composite veins are systematically cut by veins exclusively filled by carbonate (Figure 5g). At the contact with carbonate veins (up to 1 mm from the vein wall; Figures 5f and 6e), the siliciclastic rocks are characterized by mm-thick alteration selvages consisting of corroded quartz grains surrounded by late carbonate cement (Figure 6f). Moreover, pyrophyllite, chalcopyrite, rutile, smectite, baryte, apatite, and illite are also observed within the carbonate cement in the selvages of the siliciclastic rocks (Figures 6f–6i).

Carbonate veins within the Triassic dolostones (thrust hanging wall) are up-to-1 cm wide. At the thin section scale, they show blocky or elongated-blocky syntaxial textures (Figure 5e). The carbonates commonly have mixed dolomite-ankerite composition (Figure 6a) and are associated with pyrite, baryte, rutile, and monazite (Figures 6a–6e). Pyrite is commonly euhedral (Figures 6b, 6d and 6e) with grain size up to a few millimeters.

#### 4.3. Microthermometry and Element Mapping of Fluid Inclusions

Primary FIs were measured in both quartz veins and carbonate mineralizations at the thrust hanging wall and footwall. Primary FIs in quartz have diameters mostly between 5 and 30  $\mu\text{m}$  and contain liquid water and vapor (LV) (Figures 7a and 7b). Secondary FIs (i.e., occurring along intra-grain trails and/or trapped in microfractures) contain LV and were measured only in quartz crystals (Figure 7a). Primary FIs in quartz veins show a wide range of ice melting temperatures ( $T_{\text{m,ICE}}$ ), ranging from  $-17.5^\circ\text{C}$  to  $-1.5^\circ\text{C}$  (Figure 7c), corresponding to salinities ranging from 2 to 20 wt % NaCl equivalent (Figure 7g). We observe a bimodal distribution of  $T_{\text{m,ICE}}$  with one group having values between  $-15.5^\circ\text{C}$  and  $-11^\circ\text{C}$ , and another group between  $-3.5^\circ\text{C}$  and  $-1.5^\circ\text{C}$  (Figure 7c). Homogenization temperatures ( $T_{\text{h,LV-L}}$ ) of primary FIs in quartz show a wide range, spanning from  $\sim 232^\circ\text{C}$  to  $\sim 350^\circ\text{C}$  and a bimodal distribution (Figure 7e). Secondary FIs show a range of  $T_{\text{m,ICE}}$  values from  $-24.5^\circ\text{C}$  to

**Figure 5.** (a) Microphotograph under cross-polarized light showing the mineralogical composition of the siliciclastic rocks essentially consisting of quartz grains. Note the carbonate veins with agglomerate texture and arranged sub-perpendicular to  $S_0$  (see Figure 4b for sampling location). (b) Microphotograph under cross-polarized light showing small variations in grain size of quartz grains marking the faint planar anisotropy which corresponds to the bedding ( $S_0$ ). (c) Microphotograph under cross-polarized light of white micas and microcrystalline quartz aligned along incipient foliation planes ( $S_1$ ) parallel to  $S_0$ . (d) Microphotograph under cross-polarized light showing the brecciated layers within the Triassic dolostone. The brecciated layer consists of fragments of dolostones embedded within carbonate cement (see Figure 4d for sampling location). (e) Microphotograph under cross-polarized light showing the recrystallized Triassic dolostone and detail of a carbonate vein filled by elongated-blocky crystals (see Figure 4d for sampling location). (f) Microphotograph under cross-polarized light of a siliciclastic rock-hosted quartz vein. Note that such vein is brecciated (with carbonate cement) and is also cut by carbonate vein. The thickness of the thin section is of about 80–100  $\mu\text{m}$  to preserve both carbonate and quartz as they are characterized by a strongly different hardness. (g) Microphotograph under polarized light showing crosscutting relationships between carbonate veins which cut the composite veins (see panel (f)). Note that the composite veins are made up of early segregated quartz from the vein walls toward the center and late carbonate precipitation at the center of the vein. (h) Microphotograph under cross-polarized light showing the agglomerated (or very fine-grained) texture of carbonate veins within the siliciclastic rocks (see Figure 4b for sampling location). (i) Microphotograph under cross-polarized light of blocky carbonate veins within the siliciclastic rocks.



**Figure 6.** Scanning electron microphotographs of quartz and carbonate mineralizations and host rocks. (a) Carbonate vein within the siliciclastic rocks which are made up of a quartz-rich matrix (quartz grains). The carbonate vein consists of dolomite and ankerite. Pyrite and rutile occur within the carbonate vein. (b) Carbonate veins within the siliciclastic rocks. Note the euhedral crystals of pyrite associated with carbonate veins. (c) Detail of rutile and monazite in paragenesis and within the carbonate veins hosted within the siliciclastic rocks. (d) Detail of carbonate vein (hosted within the siliciclastic rocks) with associated baryte and pyrite. (e) Detail of the contact between carbonate veins and siliciclastic rocks (alteration selvage shown in Figure 5g). Note that the carbonate veins cut the quartz vein. (f) Detail of the alteration selvage of siliciclastic rocks close to the carbonate vein (see panel e). Note the carbonate cement around corroded quartz grains. Apatite and illite associated with carbonate cement are shown. (g) Detail of illite associated with carbonate cement within the alteration selvage of siliciclastic rocks close to the carbonate vein (see panel e). (h) Detail of pyrophyllite and smectite associated with carbonate cement within the alteration selvage of siliciclastic rocks close to the carbonate vein (see panel e). (i) Detail of chalcopyrite associated with the carbonate cement within the alteration selvage of siliciclastic rocks close to the carbonate vein (see panel e). Chalcopyrite shows an altered rim which is altering to iron oxides and siderite. The punctual semiquantitative chemical analyses of solid solution of dolomite and ankerite, rutile, pyrite, baryte, pyrophyllite, smectite, chalcopyrite, and altered chalcopyrite are also shown.

–17.5°C (Figure 7c), corresponding to higher salinity from 20 to 25 wt% NaCl eq. (Figure 7g). Homogenization into the liquid phase occurs at temperatures ranging from ~230°C to ~300°C (Figure 7e).

Primary FIs in carbonate mineralization in the thrust hanging wall and footwall are more abundant and smaller than primary FIs in quartz. Their sizes are variable, mostly between 5 and 25 μm in diameter, containing LV at



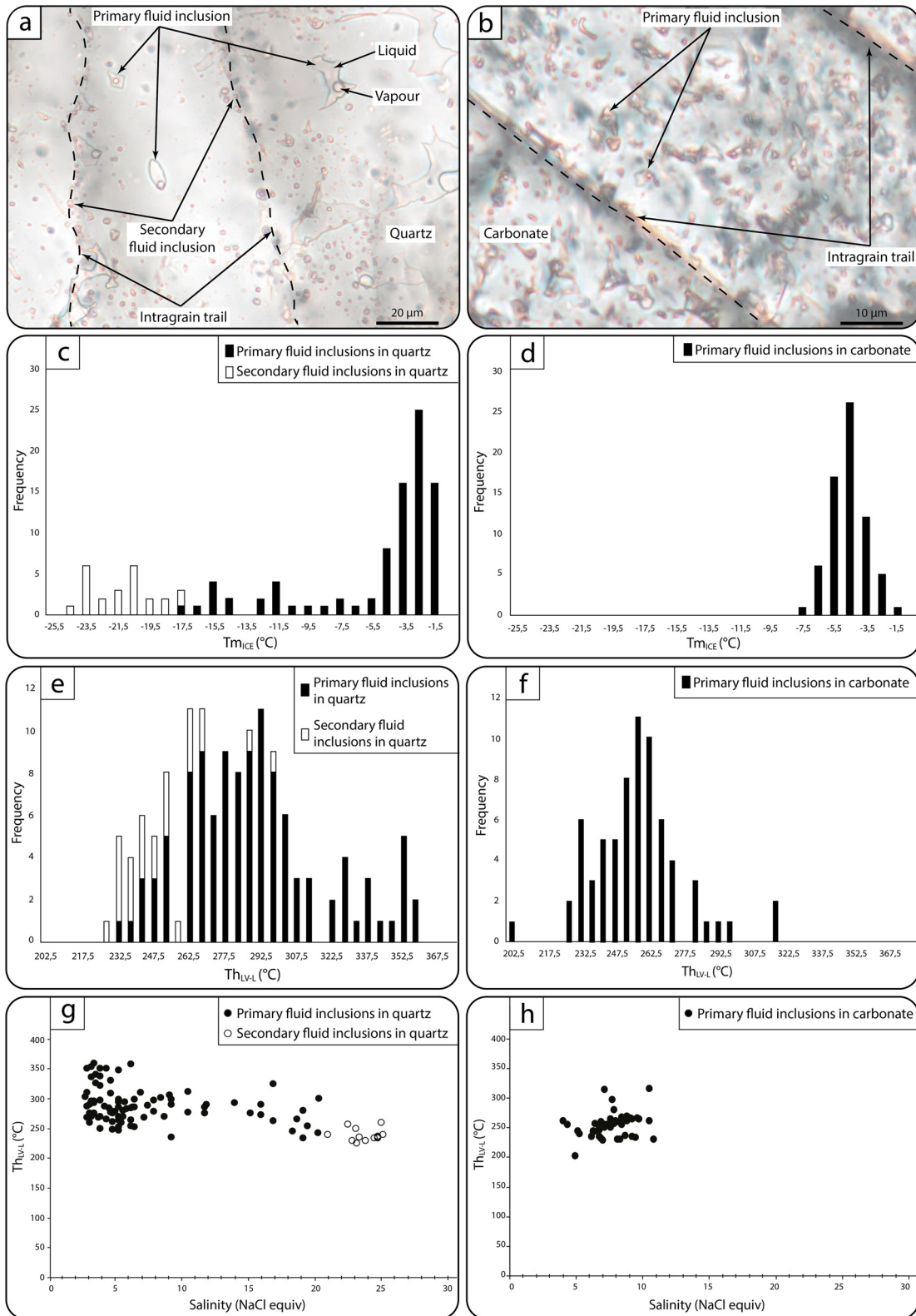


Figure 7.

room temperature (Figure 7b). They show  $T_{m_{ICE}}$  values ranging from  $-7.5^{\circ}\text{C}$  to  $-1.5^{\circ}\text{C}$  (average  $-4.5^{\circ}\text{C}$ ), with unimodal Gaussian distribution;  $T_{h_{LV-L}}$  ranges from  $\sim 202^{\circ}\text{C}$  to  $\sim 320^{\circ}\text{C}$  with an average of  $\sim 260^{\circ}\text{C}$  (Figures 7d and 7f). Their salinity varies between  $\sim 4$  and  $\sim 11$  wt % NaCl eq. (Figure 7h), overlapping the salinity field of the primary FIs in quartz veins (Figures 7g and 7h).

Precipitates from decrepitated FIs hosted by quartz veins and carbonate mineralizations are dominated by Na and Ca (Figures S1–S3 in Supporting Information S1). Cl was not detected in significant amounts (Figures S1–S3 in Supporting Information S1) due to evaporation after decrepitation. Small fragments of quartz and/or dolomite are found in the samples (Figures S1–S3 in Supporting Information S1) and may represent (a) former daughter minerals, (b) accidentally trapped crystals from the FIs, and (c) fragments of surrounding rocks that were flushed out by the fluids during decrepitation.

#### 4.4. Stable Isotope Systematics

Results from stable isotope analyses are shown in Figure 8s and listed in Tables S2 and S3 in Supporting Information S1. Results are reported in the conventional  $\delta$  notation with respect to the Vienna Pee Dee Belemnite (VPDB) for  $\delta^{13}\text{C}$  and Vienna Standard Mean Ocean Water for  $\delta^{18}\text{O}$ . Quartz veins show  $\delta^{18}\text{O}$  values between  $18.1\text{‰}$  and  $20.1\text{‰}$  (Table S2 in Supporting Information S1). No significant differences in the  $\delta^{18}\text{O}$  values are observed between sub-vertical and sub-horizontal veins (Table S2 in Supporting Information S1). The carbonate cement in siliciclastic rocks shows  $\delta^{13}\text{C}$  and  $\delta^{18}\text{O}$  values ranging between  $-0.8\text{‰}$  and  $-0.1\text{‰}$ , and between  $+14.1\text{‰}$  and  $+19.0\text{‰}$ , respectively (Figure 8a and Table S3 in Supporting Information S1). Carbonate veins within the Triassic dolostone provide two distinct groups of values, with  $\delta^{13}\text{C}$  and  $\delta^{18}\text{O}$  values ranging  $-1.1\text{‰}$  to  $-1.0\text{‰}$ ,  $+14.4\text{‰}$  to  $15.2\text{‰}$  and  $+2.7\text{‰}$  to  $+3.2\text{‰}$ ,  $+16.4\text{‰}$  to  $21.7\text{‰}$ , respectively (Figure 8a and Table S3 in Supporting Information S1). The Triassic dolostone displays  $\delta^{13}\text{C}$  and  $\delta^{18}\text{O}$  values ranging between  $+0.9\text{‰}$  and  $+2.8\text{‰}$ , and between  $+11.2\text{‰}$  and  $+21.9\text{‰}$ , respectively (Figure 8a and Table S3 in Supporting Information S1).

Clumped isotope analysis of five carbonate mineralizations hosted within the Triassic dolostone yields  $\Delta 47$  values between  $0.289\text{‰}$  and  $0.456\text{‰}$  (I-CDES; Table S4 in Supporting Information S1). Using the Anderson et al. (2021) calibration, these values correspond to temperatures between  $86^{\circ}\text{C} \pm 9^{\circ}\text{C}$  and  $262^{\circ}\text{C} \pm 9^{\circ}\text{C}$ , respectively (Figure 8a and Table S4 in Supporting Information S1). In particular, the group of carbonate mineralizations with higher  $\delta^{13}\text{C}$  and  $\delta^{18}\text{O}$  values is characterized by temperatures between  $\sim 158$  and  $\sim 262^{\circ}\text{C}$ . The group characterized by lower values of  $\delta^{13}\text{C}$  and  $\delta^{18}\text{O}$  show temperature of  $\sim 86^{\circ}\text{C}$  (Figure 8a and Table S4 in Supporting Information S1). Clumped isotope analysis of two samples from the Triassic dolostone yields  $\Delta 47$  values between  $0.288\text{‰}$  and  $0.292\text{‰}$  (I-CDES; Table S4 in Supporting Information S1). Using the Anderson et al. (2021) calibration, these values correspond to temperatures between  $256^{\circ}\text{C} \pm 8^{\circ}\text{C}$  and  $265^{\circ}\text{C} \pm 7^{\circ}\text{C}$ , respectively (Figure 8a and Table S4 in Supporting Information S1).

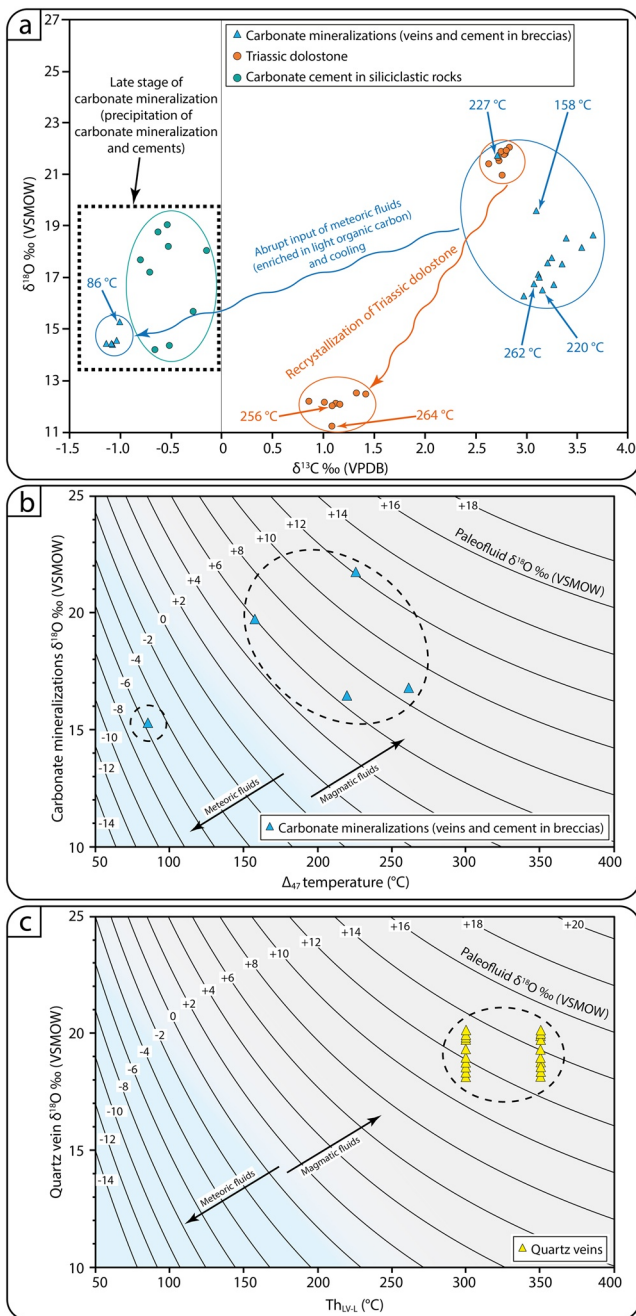
The calculated  $\delta^{18}\text{O}$  of the fluid ranges from  $-5.5\text{‰}$  to  $12.2\text{‰}$  for carbonate mineralization (Figure 8b and Table S4 in Supporting Information S1) and from  $11\text{‰}$  to  $15\text{‰}$  for quartz veins (Figure 8c). Temperature constraints for quartz veins correspond to the  $T_{h_{LV-L}}$  temperatures of  $\sim 300^{\circ}\text{C}$  and  $\sim 350^{\circ}\text{C}$  of primary FIs in quartz veins, corrected for the original pressure (see Section 5.2).

#### 4.5. Noble Gases, $\text{H}_2\text{O}$ , and $\text{CO}_2$ in Fluid Inclusions

The concentrations of noble gases (He, Ne, and Ar) and their isotopic ratios ( $^3\text{He}/^4\text{He}$ ,  $^{20}\text{Ne}/^{22}\text{Ne}$ ,  $^{21}\text{Ne}/^{22}\text{Ne}$ ,  $^{40}\text{Ar}/^{36}\text{Ar}$ , and  $^{38}\text{Ar}/^{36}\text{Ar}$ ) in FIs hosted in quartz veins and carbonate mineralizations are reported in Table 1. For the quartz veins (representative sample Z100 B2), the concentration of  $\text{H}_2\text{O}$  and  $\text{CO}_2$  and the C isotopic composition ( $\delta^{13}\text{C}$  vs. VPDB in per mil) of  $\text{CO}_2$  are also reported with a duplicate measurement. The mean concentration of  $\text{H}_2\text{O}$  is  $1.34 \times 10^{-5}$  mol/gr, while that of  $\text{CO}_2$  is  $1.56 \times 10^{-7}$  mol/gr, indicating that water is the dominant species

**Figure 7.** (a) Primary and secondary fluid inclusions (FIs) in quartz veins arranged along intragrain trails and trapped in microfractures. (b) Primary FIs in carbonate mineralizations (c–h) Microthermometric data from analysis of crystal FIs. (c) Histogram of ice melting temperatures of primary and secondary FIs in quartz veins sampled from siliciclastic rocks. (d) Histogram of ice melting temperature of primary FIs in carbonate sampled from dolostone. (e) Histogram of liquid–vapor homogenization temperatures of primary and secondary FIs in quartz sampled from siliciclastic rocks. (f) Histogram of liquid–vapor homogenization temperatures of primary FIs in carbonate sampled from dolostone. (g) Plot of salinity (as wt% NaCl equivalent) versus homogenization temperatures for primary and secondary FIs in quartz sampled from siliciclastic rocks. (h) Plot of salinity (as wt% NaCl equivalent) versus homogenization temperatures for primary FIs in carbonate samples from dolostone.





**Figure 8.** (a)  $\delta^{13}\text{C}$  (PDB) versus  $\delta^{18}\text{O}$  (SMOW) diagram for carbonate mineralizations (veins and cement in fault breccias), host rocks (i.e., Triassic dolostone), and carbonate cement in siliciclastic rocks. Clumped isotope temperature for carbonate mineralizations is shown. (b)  $\delta^{18}\text{O}$  (Vienna Standard Mean Ocean Water, VSMOW) versus clumped isotope temperature ( $\Delta_{47}$ ) for carbonate mineralizations. The curves represent the paleofluid  $\delta^{18}\text{O}$  (VSMOW) compositions as a function of temperature and have been constructed using the equation of Müller et al. (2019). (c)  $\delta^{18}\text{O}$  (VSMOW) versus  $T_{\text{HVL}}$  for quartz veins. The curves represent the paleofluid  $\delta^{18}\text{O}$  (VSMOW) compositions as a function of temperature and have been constructed using the equation of Clayton et al. (1972). Temperature constraints ( $\sim 300^\circ\text{C}$  and  $\sim 350^\circ\text{C}$ ) for quartz veins are represented by the temperature of primary FIs in quartz veins corrected for the original pressure (see Section 5.2).

of the FIs. The  $^4\text{He}$  concentration in the carbonate mineralization (from  $1.47 \times 10^{-11}$  to  $5.61 \times 10^{-12}$  mol  $\text{g}^{-1}$ ) are higher than in the inclusions in quartz (from  $1.02 \times 10^{-12}$  to  $4.93 \times 10^{-13}$  mol  $\text{g}^{-1}$ ). The  $^{20}\text{Ne}$  concentrations in the FIs of the two different kinds of mineralization (carbonate vs. quartz) show the same behavior as  $^4\text{He}$ , being from  $1.47 \times 10^{-13}$  to  $9.79 \times 10^{-14}$  mol  $\text{g}^{-1}$  and from  $4.54 \times 10^{-14}$  to  $9.04 \times 10^{-14}$  mol  $\text{g}^{-1}$ , respectively (Table 1). Most of the  $^4\text{He}/^{20}\text{Ne}$  ratios in the carbonate mineralization (57–100) are higher than those in quartz (4–43; Figure 9a). In contrast, the concentration of  $^{40}\text{Ar}$  in the two types of mineralization (quartz vs. carbonate) is in a range of one order of magnitude (from  $1.94 \times 10^{-11}$  to  $1.92 \times 10^{-10}$  mol/gr; Table 1). The He isotopic ratio (expressed as R/Ra, where Ra is the He isotopic ratio in atmosphere,  $1.39 \times 10^{-6}$ ) varies from 0.04 to 1.62Ra, with the lowest values in the carbonate mineralization (Table 1, Figure 9a). The highest He concentrations are found in the samples showing the lowest  $^3\text{He}/^4\text{He}$  ratios (Figure 9a). The  $^{20}\text{Ne}/^{22}\text{Ne}$  (from 9.81 to 9.90) and  $^{21}\text{Ne}/^{22}\text{Ne}$  (from 0.0291 to 0.0297) are very close to or overlap the ratios found in air (9.8 and 0.029 respectively; Figure 9a). The  $^{40}\text{Ar}/^{36}\text{Ar}$  ratios are from 396 to 894, higher than the ratio in air (298.6; Lee et al., 2006). The  $^{38}\text{Ar}/^{36}\text{Ar}$  is similar to that in air (0.1885), within the limits of the analytical uncertainty. The mean values of  $\delta^{13}\text{C}_{\text{CO}_2}$  for quartz veins (representative sample Z100 B2) is  $-0.1\text{‰}$ .

## 5. Discussion

### 5.1. Tectono-Structural Scenario

Our field and microstructural observations allow the identification of at least two main events of mineralization assisted by post-orogenic extensional tectonics. From the observed cross-cutting relationships (Figure 5f), it is evident that the first event was localized at the footwall of the thrust and led to the formation of quartz veins and conversion of detrital smectite and kaolinite to illite and pyrophyllite, respectively. The second event caused carbonate (and rutile, monazite, chalcopyrite, baryte, and smectite) precipitation both at the hanging wall and footwall of the thrust. The second carbonate veining event has been dated to late Messinian-early Pliocene time by U-Pb carbonate geochronology (Curzi et al., 2020).

The set of variably oriented subvertical quartz veins (Figures 4b and 4c) is coherent with a stress field where the maximum effective stress  $\sigma_1$  is vertical and  $\sigma_2$  and  $\sigma_3$  are horizontal and tensile ( $\sigma_3 \leq \sigma_2 < 0$ ; e.g., Li & Ji, 2021). The occurrence of a sub-horizontal set of quartz veins (Figure 4a) which reactivates the primary bedding at the footwall of the thrust contact in an extensional regime suggests that hydrostatic pressure was (supra)lithostatic (Shen et al., 2020), as also attested by the blocky texture in quartz veins (e.g., Hilgers & Urai, 2002; Figure 5f).

Variably oriented carbonate veins and cement occur within crackle and chaotic breccias localized adjacent to the normal faults (Figures 4d–4f and 5d). These carbonates precipitated under high fluid pressure conditions, here hypothesized to correspond to episodic events of high strain rate, implosive brecciation (Figures 4d–4f) and subsequent rapid fluid depressurization (Mort & Woodcock, 2008; Sibson, 2000; Woodcock et al., 2014).

### 5.2. P-T-X Environment of Quartz Mineralizations

Primary FIs in quartz veins have homogenization temperatures ranging between  $\sim 232^\circ\text{C}$  and  $\sim 350^\circ\text{C}$  (Figures 7e and 10a). By considering the

**Table 1**  
Summary of Concentrations of Noble Gases in Fluid Inclusions in Quartz Veins and Carbonate Mineralizations

Sample	Type	<sup>20</sup> Ne mol/g	<sup>20</sup> Ne err	<sup>4</sup> He mol/g	<sup>4</sup> He err	He/Ne	R/Ra	Rc/Ra
Z116	Carbonate mineralization	1.47E-13	0.64	1.47E-11	0.03	100.0	0.04	0.04
Z115	Carbonate mineralization	9.79E-14	0.78	5.61E-12	0.04	57.3	0.19	0.19
Z100 A1	Quartz vein	4.54E-14	0.76	4.93E-13	0.03	10.8	1.46	1.49
Z100 A2	Quartz vein	9.04E-14	0.70	3.89E-12	0.02	43.0	0.95	0.95
Z100 B1	Quartz vein	8.94E-14	0.63	1.02E-12	0.02	11.4	1.62	1.65
Z100 B2	Quartz vein	8.36E-14	0.69	3.18E-13	0.01	3.8	0.44	0.42

maximum pressure of ~200 MPa (Curzi et al., 2020) experienced by the siliciclastic rocks that hosted the quartz veins during contractional tectonics, a maximum lithostatic pressure of ~150 MPa is estimated for the entrapment of the FIs (Figure 10a). Assuming a geothermal gradient of 60°C km<sup>-1</sup> (Figure 10a), typical of high-heat flow conditions in back-arc environments such as those presently recorded along the peri-Tyrrhenian margin (Diaferia et al., 2019), and by considering that the quartz veins developed under fluid overpressure (see Section 5.1), we estimated quartz precipitation pressures ranging between ~125 and ~150 MPa (Figure 10a). Hence, applying the pressure correction, precipitation temperatures between ~300°C and ~350°C are estimated (Figure 10a).

The δ<sup>18</sup>O of quartz veins (Table S2 in Supporting Information S1) and the calculated fluid δ<sup>18</sup>O values ranging between 11‰ and 15‰ (Figure 8c), suggest a magmatic origin for the mineralizing fluids (e.g., Yan et al., 2020). This is consistent with the (a) high temperature of quartz crystallization (>300°C), (b) high fluid salinities (Figure 7g), (c) high contents of Na and Ca observed from decrepitated FIs (Figures S2 and S3 in Supporting Information S1), and (d) the He isotopic signature of FIs in quartz veins suggesting a mantle-derived component (Figure 9a; Section 5.2). Furthermore, the relatively small variation of δ<sup>18</sup>O values of quartz veins (from 18‰ to 20‰; Table S2 in Supporting Information S1) is interpreted as reflecting the very limited oxygen isotope exchange between magmatic fluids and surrounding rocks (e.g., Yan et al., 2020). This is consistent with the rapid fluid flow associated with fluid overpressure events responsible for the precipitation of quartz veins (Figures 10a and 11a) and the He isotopic signature of FIs that preserves a mantle-derived component (Figure 9a).

### 5.3. *P-T* Environment of Carbonate Mineralization

Carbonates precipitated in the footwall and hanging wall of the thrust document pervasive fracturing and fluid infiltration at depths shallower than those related to quartz veining. Primary FIs in carbonates record minimum trapping temperatures between ~202°C and ~320°C (Figure 7f). Using the temperatures derived from clumped isotopes and a geothermal gradient of 60°C km<sup>-1</sup>, a pressure range of ~25 MPa (~240°C) to ~120 MPa (~320°C) is estimated for the entrapment of the FIs in carbonates (Figure 10b). The range of temperatures between ~320°C and ~240°C likely corresponds to the transition from high *P-T* closed-system conditions at a minimum lithostatic pressure of ~120 MPa; to lower temperature open-system conditions at hydrostatic pressure (Figure 10b; Selverstone et al., 2012). The temperatures from clumped isotopes, between ~262°C and 86°C (Figure 8a), are interpreted as cooling temperatures associated with the opening of the fluid system and an increasing input of meteoric fluids and late stage carbonate mineralization (See Section 5.5; Figure 10b). Hence, the minimum *P-T* conditions recorded by FIs in carbonate minerals, does not correspond with the minimum *T* conditions estimated by clumped isotopes (Figure 10b).

### 5.4. Noble Gases Geochemistry of Mineralizing Fluids

The analytical procedure of single step in vacuo crushing cannot distinguish different generations of FIs within the mineralization (Kendrick & Burnard, 2013; Stuart et al., 1994). Hence, the noble gas compositions are an average of the different generations of FIs present in the studied mineralizations. However, this procedure strongly limits the release of noble gases from the mineral matrix and the contamination of the noble gases trapped in the inclusions by those produced in the matrix over time (post entrapment modifications such as addition of cosmogenic <sup>3</sup>He, radiogenic <sup>4</sup>He and <sup>40</sup>Ar) is often negligible. Furthermore, in quartz and carbonates a significant production of radiogenic <sup>4</sup>He by the decay of U and Th can be excluded because of their low concentrations



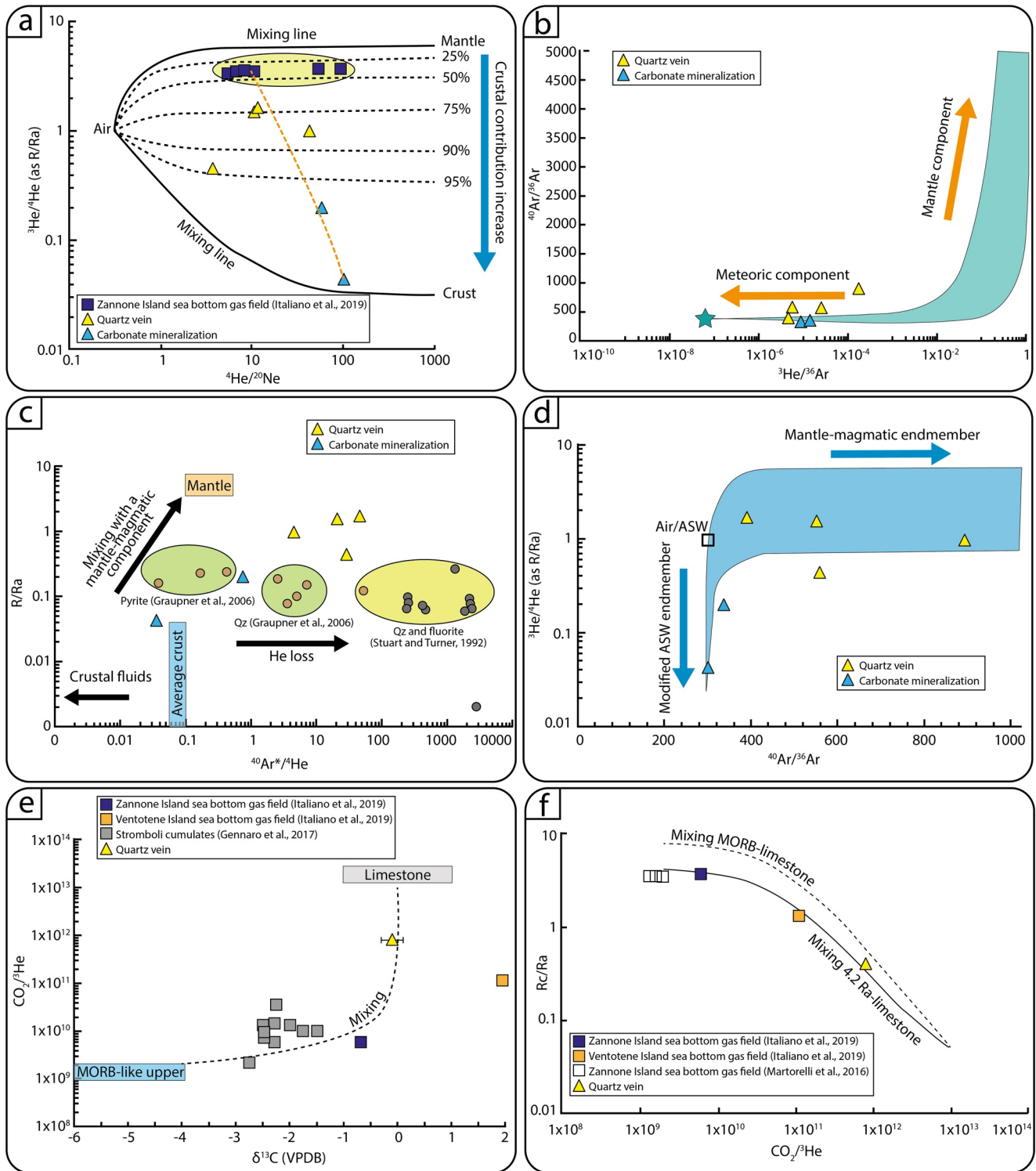
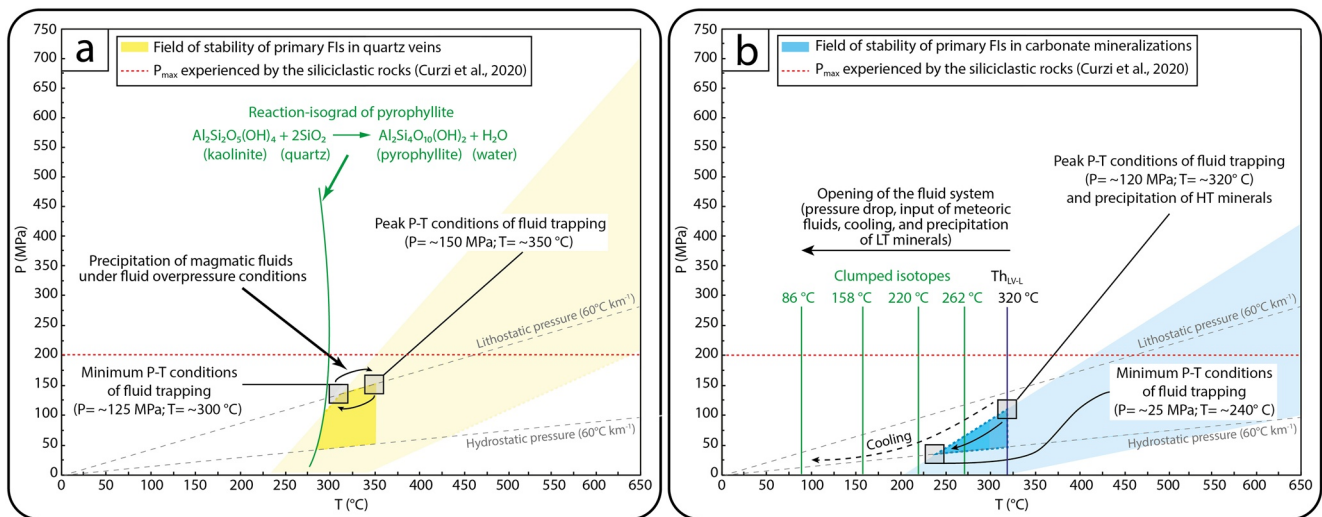


Figure 9.

in our samples (Curzi et al., 2020) and the young age of the mineralizations (maximum  $\sim 7$  Ma). The minerals are also K free and in situ radiogenic  $^{40}\text{Ar}$  is proven to be negligible (Stuart et al., 1995). Modification of the He and Ar isotopic signature in FIs can occur through loss or addition of noble gases due to post mineralization processes. However, the lack of correlation between noble gases concentrations, elemental and  $^3\text{He}/^4\text{He}$



**Figure 10.** (a) Field of  $P$ - $T$  trapping conditions for primary fluid inclusions (FIs) in quartz veins. (b) Field of  $P$ - $T$  trapping conditions for primary FIs in carbonate mineralizations. The dashed gray lines are lithostatic and hydrostatic geothermal gradients for  $60^\circ C km^{-1}$ . The yellow (in panel (a)) and blue (in panel (b)) areas represent the whole  $P$ - $T$  trapping conditions estimated through isochores. The dark yellow and blue areas identify the  $P$ - $T$  trapping ranges constrained by the overlapping of FIs isochores,  $P_{max}$  experienced by the host rocks (siliciclastic rocks; Curzi et al., 2020), mineral paragenesis associated with alteration processes, and clumped isotopes temperatures for carbonate mineralizations. Quartz veins in panel (a) precipitated under fluid overpressure conditions, with fluid pressure equal to lithostatic pressure and comprised between  $\sim 125$  and  $\sim 150$  MPa, and temperatures between  $\sim 300^\circ C$  and  $\sim 350^\circ C$ . Carbonate mineralizations in panel (b) precipitated in an evolving fluid system first characterized by fluid overpressure conditions, with fluid pressure equal to lithostatic pressure ( $\sim 100$  MPa) at a temperature of  $\sim 320^\circ C$ , and in which HT minerals (monazite, rutile, and chalcopyrite) precipitated within the alteration selvages of the host rocks. The fluid system evolved through time into an open fluid system and associated pressure drop and cooling in which the minimum  $P$ - $T$  condition of carbonate precipitation occurred at a  $\sim 30$  MPa pressure and  $\sim 254^\circ C$  temperature, and in which LT minerals (barite and smectite) began to precipitate within the alteration selvages of the host rocks.

ratios suggests that late modifications are negligible. Instead, a positive correlation between He concentration and  $^4He/^{20}Ne$  ( $R^2 = 0.96$ ) can be observed (Figure S5a in Supporting Information S1), with the highest values of the latter ratio observed in carbonate mineralizations. When comparing  $^4He/^{20}Ne$  with  $^{40}Ar/^{36}Ar$  (Figure S5a in Supporting Information S1), it can be noted that only carbonate mineralizations fall along a mixing curve between an atmospheric ( $^4He/^{20}Ne = 0.318$  and  $^{40}Ar/^{36}Ar = 296.6$ ) and a hypothetical mantle or crustal component that is characterized by high  $^4He/^{20}Ne \sim 1,000$  and  $^{40}Ar/^{36}Ar \sim 10,000$ . Instead, quartz veins show  $^4He/^{20}Ne$  values apparently lower than expected by the mixing path (Figure S5b in Supporting Information S1). It must be noted that the mixing path would not change significantly if higher  $^4He/^{20}Ne$  and  $^{40}Ar/^{36}Ar$  values are assumed. This indicates that quartz veins may have suffered a partial loss of He. Shuster and Farley (2005) highlighted that He may diffuse from the crystal lattice of quartz, especially at temperatures next to or above  $400^\circ C$ , which could have happened at the crystallization temperature  $>300^\circ C$  of our samples (see Section 5.5). However, the diffusivity of  $^4He$  across quartz seems indistinguishable from that of  $^3He$  (Shuster & Farley, 2005), implying that even in the case of a diffusive loss of He, the  $^3He/^4He$  should maintain the original signature. Therefore, we argue that the He and Ar isotopic ratios in the FIs of the quartz veins and carbonate mineralizations represent the signatures of the ore-forming fluids at the time of trapping.

**Figure 9.** (a) Helium isotopes as  $R/Ra$  ( $R$  is the  $^3He/^4He$  of the sample and  $Ra$  is the He isotopic signature in air) versus the  $^4He/^{20}Ne$  ratios. The black lines represent the mixing between the air end member ( $1Ra$ ,  $^4He/^{20}Ne$  ratio = 0.318) and Mantle ( $6.3Ra$ ,  $^4He/^{20}Ne$  ratio  $>1,000$ ) and crust ( $0.01$ – $0.03Ra$ ;  $^4He/^{20}Ne$  ratio  $>1,000$ ). All the references are cited in the manuscript. The black dotted lines represent the mixing between air and different deep end members that result combining in different percentages the two mantle and crustal end members. The orange dotted line is the best fit between the samples of Zannone Island and the average He isotopic signature in the fluids emitted from the local submarine volcanic-hydrothermal gas emissions. (b)  $^3He/^{36}Ar$  versus  $^{40}Ar/^{36}Ar$  plot. The blue area is consistent with a mixing between mantle-magmatic fluids that are enriched in  $^{40}Ar$  and  $^3He$  and a fluid with air or air saturated water (the blue star:  $^3He/^{36}Ar = 1 \times 10^{-8}$  and  $^{40}Ar/^{36}Ar = 296.6$ ; Kendrick & Burnard, 2013). The blue area is built by plotting literature data of Figure 3 and it is representative of the mixing (Kendrick & Burnard, 2013 and references therein; Tang et al., 2017; Goodwin et al., 2017; Wu et al., 2018). (c) He-Ar isotopes systematics of fluid inclusions (FIs) in quartz and dolomite. The blue area is built plotting data from previous investigations of FIs with both magmatic and crustal origins in various worldwide ore deposits (literature data of Figure 9b). The blue filled square represents the Air and Air Saturated Water end members. The Modified Air endmember is an air saturated water that is simply enriched by addition of radiogenic  $^4He$  (Burnard et al., 1999). (d)  $5^{40}Ar^*/4He$  versus  $^3He/^4He$  (as  $R/Ra$ ) plot. The composition of the three fields: (1) Average crust, (2) the low crustal fluids, and (3) mantle are from Kendrick and Burnard (2013). The gray area is the field of the mixing between the crustal fluids and mantle-magmatic fluids. This area is built by plotting data in the literature used in Figures 9b and 9c. (e)  $\delta^{13}C$  versus  $CO_2/^{3}He$ ; (f)  $CO_2/^{3}He$  versus  $^3He/^4He$  (as  $R/Ra$ ).



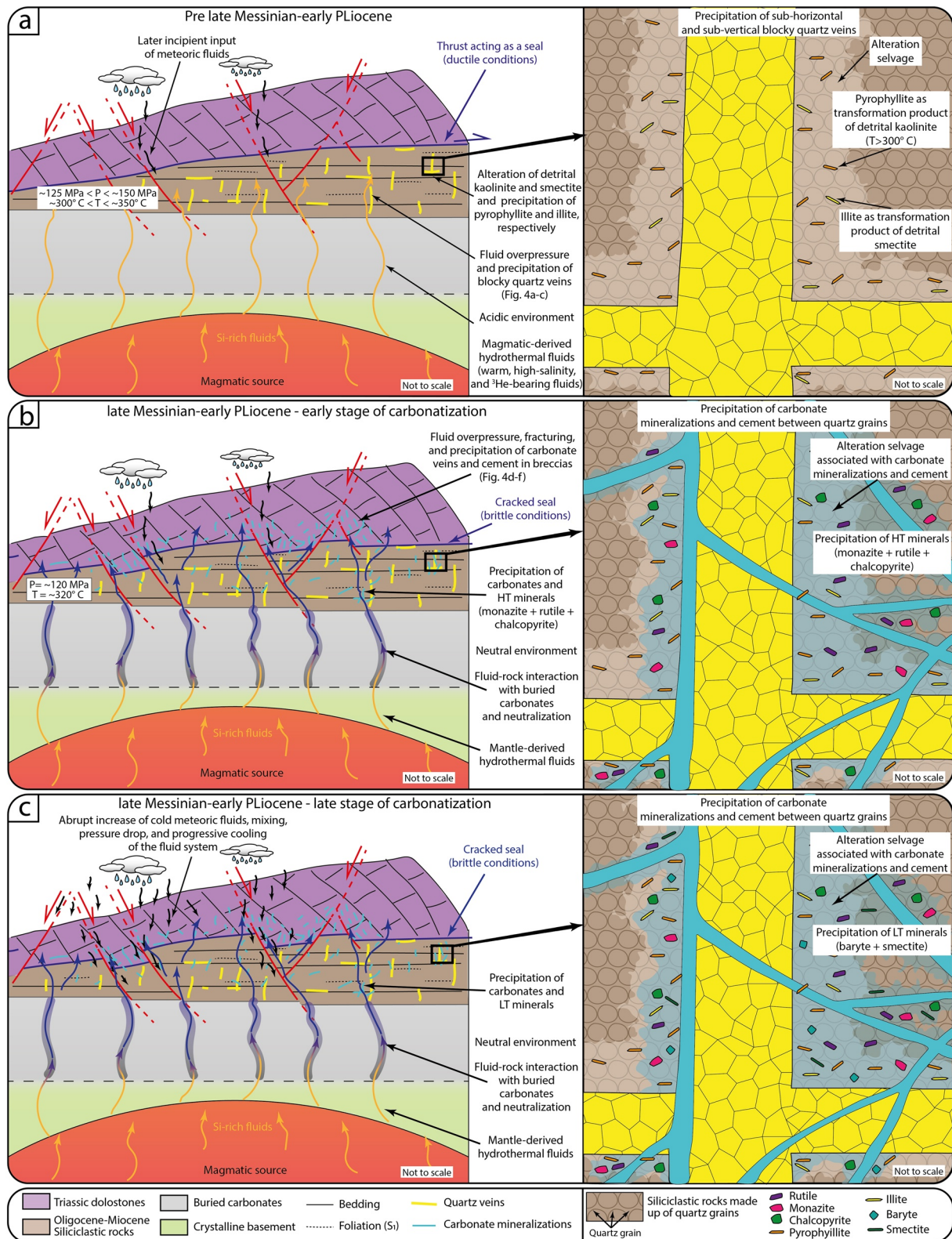


Figure 11.

### 5.5. Mixing Processes: Evidence From Noble Gases

He in natural fluids is generally sourced from the atmosphere, mantle and crust. The  $^3\text{He}/^4\text{He}$  ratios of these three sources are significantly different, hence this tracer is a powerful tool for recognizing the origin of natural fluids. The upper convective mantle reservoirs  $^3\text{He}/^4\text{He}$  ratio is between  $\sim 6.3$  Ra (SCLM, Sub Continental Lithospheric Mantle; Gautheron et al., 2005) and  $\sim 7$  to 9 Ra (MORB, Mid Ocean Ridge Basalt; Graham, 2002). In contrast, the He isotopic signature in crustal fluids is dominated by radiogenic  $^4\text{He}$ ,  $\sim 0.01$  to 0.03 Ra (Ballentine et al., 2002). Furthermore, both the  $^4\text{He}/^{20}\text{Ne}$  and  $^{40}\text{Ar}/^{36}\text{Ar}$  ratios of these end-members are different, being 0.318 in air and  $>1,000$  in the crust and mantle (Sano & Wakita, 1985), and 298.6 in air and  $>>298.6$  up to 44,000 in the crust and the mantle (Lee et al., 2006; Ozima & Podosek, 2002), respectively. Therefore, according to the approach proposed by Sano and Wakita (1985), by combining  $^3\text{He}/^4\text{He}$  and  $^4\text{He}/^{20}\text{Ne}$  ratios in mixing equations it is possible to solve the contribution of the atmospheric, crustal and mantle-derived He in the natural fluids. If we assume the He isotopic ratio of the European Sub Continental Lithospheric Mantle (SCLM;  $6.3 \pm 0.3$ ; Gautheron et al., 2005) as representative of the mantle beneath the study area, the computed mantle-component in the fluids that are trapped in quartz inclusions is up to 28% (Figure 9a).

The  $^3\text{He}/^4\text{He}$  versus the  $^4\text{He}/^{20}\text{Ne}$  relationship shows that the fluids trapped within the mineralizations of ZI could result from a three-component mixing (orange dotted line in Figure 9a) between (a) a crustal component that is dominated by a radiogenic He isotopic signature (0.01–0.03Ra; entirely sustained by  $^4\text{He}$  produced by radiogenic decay of U and Th), as shown by carbonate mineralizations, (b) a Zannonne-type magmatic component (average He isotopic ratio up to 3.7 Ra; yellow area in Figure 9a) estimated from the He isotopic signature in the sea bottom outgassing fluids (Italiano et al., 2019; Martorelli et al., 2016), and (c) a very low atmospheric component.

The  $^3\text{He}$  and  $^{36}\text{Ar}$  are both unradiogenic and their ratio in the pure air saturated water is  $5 \times 10^{-8}$ , whose  $^{40}\text{Ar}/^{36}\text{Ar}$  ratio is 298.6 (Figure 9b). Therefore, combining the  $^3\text{He}$  and  $^{36}\text{Ar}$  and the  $^{40}\text{Ar}/^{36}\text{Ar}$  results is possible to investigate the occurrence of an air-saturated water component together with crustal and magmatic fluids in the mineralization. The fluids trapped in the carbonate mineralizations have a He isotopic signature that is typical of the crustal fluids ( $R/Ra < 0.1$ ) and a  $^{40}\text{Ar}/^{36}\text{Ar}$  ratio (335; Table 1, Figure 9b) slightly higher than in air or volatiles dissolved into groundwater (296.6; Figure 9b). In contrast the  $^{40}\text{Ar}/^{36}\text{Ar}$  ratios in the quartz FIs (up to  $\sim 890$ ) are higher than those in atmosphere related fluids (298.6; Lee et al., 2006) since an excess of radiogenic  $^{40}\text{Ar}$  is associated with a contribution of magma-derived He ( $R/Ra$  up to 1.65). The trend in Figure 9b, indicates that fluids trapped in carbonate veins are along mixing lines between a pure air-saturated water end member and a magmatic/mantle-derived component, supporting the evidence from  $^4\text{He}/^{20}\text{Ne}$  versus  $R/Ra$  ratios. Fluids trapped in quartz veins plot slightly off the mixing lines, due to preferential loss of He with respect to Ar (Kendrick & Burnard, 2013). Indeed, it is common that FIs in quartz have anomalously He/Ar ratios (Stuart & Turner, 1992), since He is more prone to leakage than Ar in many geological materials (Graupner et al., 2006; Kendrick et al., 2011; Figure 9c).

In general, both  $^3\text{He}/^4\text{He}$  and  $^{40}\text{Ar}/^{36}\text{Ar}$  compositions conform with those reported from ore-deposits in a range of different geological settings. Thus, hydrothermal fluids are likely to retain their noble gas isotopic signature of different sources (mantle-magmatic, crust, and atmosphere) and they may be combined in different proportions representative of two possible formation-environments (e.g., orogenic ore-deposits vs. intrusion-related ore deposits; Kendrick & Burnard, 2013; Tang et al., 2017).

In absence of a preferential leakage of He, the ratio between the radiogenic crustal  $^4\text{He}$  and  $^{40}\text{Ar}^*$  is expected to be equal to the crustal production ( $^{40}\text{Ar}^*/^4\text{He} \sim 0.1\text{--}0.2$ ; Kendrick & Burnard, 2013). If FIs also contain a mantle derived component, the  $^{40}\text{Ar}^*/^4\text{He}$  ratios reflect a mixing of the two components (crust vs. mantle; e.g., and 2009; Kendrick & Burnard, 2013). This is documented in FIs in pyrite of different ages (a lot less than hundreds of millions of years; Kendrick & Burnard, 2013). Pyrite preserves Ar and He trapped in the FIs over time, so

**Figure 11.** Conceptual model for fluid circulation, fluid-rock interaction, veining, mineralization, and alteration. The upper portion of the geological cross section (siliciclastic rocks and Triassic dolostone) corresponds to the outcrop of Figure 3. (a) Before late Messinian-early Pliocene, sub-vertical and sub-horizontal quartz veins developed in the footwall of the thrust (i.e. within the siliciclastic rocks) during fluid overpressure events with uprising warm hydrothermal fluids of magmatic origin. (b) In the late Messinian-early Pliocene, the interaction between the uprising fluids with buried carbonates was responsible for change composition and precipitation of carbonate mineralizations (veins and cement in fault breccias) and carbonate cement between the quartz grains of the siliciclastic rocks. HT minerals (monazite, rutile, and chalcopyrite) are associated with carbonate precipitation. (c) During the progressive extensional tectonics (late Messinian-early Pliocene time), fracturing and mixing with downwelling meteoric fluids occurred. Carbonate veins and cement precipitated with associated low-temperature minerals (baryte and neo-forming smectite).



the  $^{40}\text{Ar}^*/^4\text{He}$  ratios coupled to the He isotopic ratios show clear mixing trends between crustal and mantle derived fluids (Hu et al., 2009). Previous studies of noble gases in quartz FIs showed preferential loss of He (Goodwin et al., 2017; Graupner et al., 2006; Stuart & Turner, 1992), thus, the resulting high values of  $^{40}\text{Ar}^*/^4\text{He}$  ratios in the trapped fluids are far from a trend of direct mixing between crustal and mantle components (Figure 9c). The  $^{40}\text{Ar}^*/^4\text{He}$  ratios in the FIs in the Zannone quartz veins are extremely high confirming a significant He loss (Figure 9c). These  $^{40}\text{Ar}^*/^4\text{He}$  ratios are not representative of the pristine ratios and, by combining the  $^{40}\text{Ar}^*/^4\text{He}$  ratios and He isotopic ratios, no mixing trend is observed. The lowest He isotopic ratio (0.04Ra) in the carbonate mineralization is associated with a  $^{40}\text{Ar}^*/^4\text{He}$  ratio (0.04) that is lower than the value caused by crustal production (0.1–0.2) and it is in the field of crustal fluids (Figure 9c; Kendrick & Burnard, 2013) supporting that the carbonate mineralization was mainly fed by crustal fluids mixed with meteoric fluids.

### 5.6. Mixing Processes: Evidence From Carbon Isotopic Composition of $\text{CO}_2$ in Fluid Inclusions

The  $\delta^{13}\text{C}_{\text{CO}_2}$  in FIs was measured only in one quartz vein (Figure 9e), yielding a value of  $-0.1\%$ . Considering the relationships between  $\delta^{13}\text{C}$ , Rc/Ra and the  $\text{CO}_2/^3\text{He}$  ratios (Figures 9e and 9f) we propose a model for the origin of  $\text{CO}_2$  and He. Following the approach by Sano and Marty (1995), the data in Figure 9e allow us to distinguish among three possible sources: (a) a SCLM-like mantle having  $\delta^{13}\text{C} \sim -4\%$  and  $\text{CO}_2/^3\text{He} \sim 2 \times 10^9$ ; (b) an inorganic carbon (limestone) having  $-1\% < \delta^{13}\text{C} < +1\%$  and  $\text{CO}_2/^3\text{He} \sim 1 \times 10^{13}$ ; and (c) an organic carbon having  $\delta^{13}\text{C} \sim -25\%$  and  $\text{CO}_2/^3\text{He} \sim 1 \times 10^{13}$ . In Figure 9e, we also report comparative gas samples collected from submarine emissions in the offshore of Zannone and Ventotene islands (Italiano et al., 2019; Figure 2a), and FIs in mantle cumulates from Stromboli (Gennaro et al., 2017; Figure 1a) that were interpreted to record a recycled inorganic carbon from the Ionian slab. The average  $\delta^{13}\text{C}$  value measured in our FIs falls on the binary mixing between mantle and limestone. The most magmatic samples of ZI (quartz veins) fall along the same trendline (Italiano et al., 2019; Figure 9e), while the submarine gas of Ventotene Island has a  $\delta^{13}\text{C}$  slightly higher than the marine limestone range, which suggests the occurrence of secondary processes (e.g.,  $\text{CO}_2$  fractionation in water). Similar indications arise from the  $\text{CO}_2/^3\text{He}$  versus Rc/Ra plot (Figure 9f), in which two binary mixing curves are plotted: (a) a MORB-like mantle having  $\text{CO}_2/^3\text{He} \sim 2 \times 10^9$  and Rc/Ra = 6.3, and a limestone having  $\text{CO}_2/^3\text{He} = 1 \times 10^{13}$  and Rc/Ra = 0.05; (b) a local magmatic source having  $\text{CO}_2/^3\text{He} = 2 \times 10^9$  and Rc/Ra = 4.2, and a limestone. Importantly, the quartz veins fall along the second binary mixing described above together with submarine gas emissions from Zannone and Ventotene islands (Figure 9f), supporting the  $\delta^{13}\text{C}$  data from FIs indicating a mixing between a local magmatic component and a crustal source. It is reasonable to suppose that at the time when quartz-mineralizing fluids were circulating, they were already mixed and that the carbonate component comes from the local sedimentary succession. This hypothesis is consistent with the presence of carbonate rocks both on ZI and within its basement (Curzi et al., 2020). We conclude that magmatic fluids of the hydrothermal system were similar to those presently degassing around ZI and were variably trapped in quartz veins and to a lesser extent in carbonate mineralizations.

### 5.7. Evolution of the Hydrothermal System

Thrusting on ZI, which occurred at  $\sim 22$  Ma, was followed by normal faulting at  $\sim 7$  Ma accompanied by volcanism and hydrothermal activity (Curzi et al., 2020; Peccerillo, 2005). During extensional tectonics, the early stages of fluid infiltration at Zannone before ca. 7 Ma were controlled by the (inherited) structural setting, dominated by the thrusting of the Triassic dolostone onto the siliciclastic rocks (Figure 11a). The fault gouge below the thrust surface acted as a low permeability seal for the uprising silica-rich magmatic fluids, leading to the increase of fluid pressure until (supra)lithostatic conditions and causing fracturing and quartz veining in the siliciclastic footwall (Figure 11a).

The infiltration of hot silica-rich fluids of magmatic origin within the structurally controlled fracture network associated with ongoing normal faulting caused a thermal overprint in the nearby siliciclastic host rocks, leading to the prograde growth of pyrophyllite and illite in the alteration selvages at the expenses of kaolinite and smectite, respectively (e.g., Frey, 1987; Figures 6f–6h, 10a and 11a), which are authigenic minerals within the siliciclastic rocks (Table S1 in Supporting Information S1). The formation of pyrophyllite at the expenses of kaolinite indicates a minimum temperature  $\sim 300^\circ\text{C}$  at 125 MPa (Figure 10a; Inoue, 1995; Larsson, 2001; Reyes, 1990; Reyes et al., 2003), consistently with the minimum temperature ( $\sim 300^\circ\text{C}$ ) estimated for the Si-rich mineralizing fluids (Figure 10a). The heat provided by uprising magmatic fluids was also responsible for the recrystallization

of the Triassic dolostones, which are characterized by two groups with different  $\delta^{13}\text{C}$  and  $\delta^{18}\text{O}$  values probably reflecting a different fluid to rock ratio during recrystallization, and clumped isotope temperatures between  $\sim 256^\circ\text{C}$  and  $264^\circ\text{C}$  (Figure 8a).

The silica-rich fluids progressively interacted (Figures 11a and 11b) with the carbonate rocks, likely causing an increase in the pH of the infiltrating fluids and final fluid neutralization (Rabiee et al., 2019; Reyes, 1990; Figures 11b and 11c). The progressive interaction of the infiltrating fluids with carbonates is further demonstrated by the dominant crustal-radiogenic component highlighted by noble gases (Figures 9a and 9c). Such fluid-rock interaction was accompanied by fluid cooling, likely facilitated by progressive embrittlement and fracturing of the host rocks (Figures 11b and 11c), and mixing with downwelling meteoric fluids along the fracture network created by normal faulting, leading to the precipitation of carbonates (Figure 11c).

The progressive deformation associated with extensional faulting promoted fluid circulation along faults (Sibson & Rowland, 2003) and abundant downflow of meteoric fluids, leading to mixing, pH changes and cooling of the hydrothermal system. The input of meteoric fluids during the late carbonate mineralization stage is also supported by the decreases of salinity in FIs in carbonates (from 11‰ to 4‰ NaCl eq; Figure 7h), and by the existence of two groups of carbonate generations with distinct  $\delta^{13}\text{C}$  and  $\delta^{18}\text{O}$  values and different formation temperature and calculated fluid compositions (Figures 8a and 8b). The group characterized by lower  $\delta^{18}\text{O}$  and negative  $\delta^{13}\text{C}$  values and colder temperature ( $\sim 86^\circ\text{C}$ ; Figures 8a and 8b) indicates the input of abundant meteoric fluids enriched in light carbon derived from oxidation of organic carbon and with a  $\delta^{18}\text{O}$  of  $-5.5\text{‰}$  (Figures 8a and 8b). This represents the latest stage of carbonate precipitation, when meteoric fluids mixed with the existing hydrothermal system during cooling (Figure 11c). The range in clumped isotope temperatures from  $\sim 262^\circ\text{C}$  to  $86^\circ\text{C}$  (Figure 8a) documents that carbonate mineralizations clearly precipitated during the cooling of the hydrothermal system (Figure 10b). The absence of transitional stages between the two groups of carbonates suggests a rapid mixing with meteoric fluids, likely due to pervasive fracturing associated with the progressive localization of extensional faulting. This is compatible with carbonate mineralization occurring in a shallow environment. Furthermore, the mineral assemblage associated with carbonate mineralizations shows a transition from high temperature assemblages (monazite, rutile, and chalcopyrite; Figures 6a, 6c and 6i) to low temperature mineral assemblages composed of barite and smectite (Figures 6f, 6f and 6h) (Larsson, 2001; Reyes et al., 2003) associated with the carbonate cement (Figures 6a, 6b, 6d, 6e and 6h; Giggenbach, 1997; Hemley & Hunt, 1992). These minerals are observed in the veins and in the carbonate cement of the  $\sim 500$  microns thick alteration selvages, where quartz grains are corroded and cemented by secondary carbonates (Figures 6a, 6c–6l and 11b and 11c). The cooling trend is also associated with a significant decrease in the  $\delta^{18}\text{O}$  composition of fluids from  $+12.2\text{‰}$  to  $-5.5\text{‰}$  (Figures 8b and 8c).

The occurrence of monazite, rutile, and chalcopyrite further confirms that hydrothermal fluids originated from a magmatic source, which provided rare Earth elements and Cu. The presence of neo-formed smectite hosted in the carbonate/ankerite mineralization (Figure 6h) also indicates mobility of K, Al, Fe, Mg, and Si in the fluids. The increase in pH of the infiltrating fluids of the hydrothermal system was likely promoted by the structurally controlled infiltration of meteoric fluids, and it is suggested as a main controlling factor of formation of the ore minerals in Zannone.

### 5.8. Linking Fossil to Active Hydrothermal System

The beginning of volcanic activity in the Zannone area has been dated at  $\sim 4.2$  Ma (Cadoux et al., 2005), while the onset of extensional tectonics on ZI was constrained to have started at about 7 Ma by U-Pb dating of the syn-tectonic carbonates associated with normal faulting and analyzed in this study (Curzi et al., 2020). We therefore propose that the hydrothermal system was active during the late Miocene, roughly coeval with the main ore stage in the Tuscan area (e.g., Brogi et al., 2011; Dini, 2003; Paoli et al., 2019; Rossetti et al., 2011; Figure 1a), and was likely fed by intrusive magmatism at depth before the onset of volcanic activity at ca. 4.2 Ma. Quartz veins and carbonate mineralizations on ZI are characterized by helium isotopic values lower than those from the adjacent volcanic areas and from the surrounding active submarine hydrothermal systems in the Pontian archipelago (Martorelli et al., 2016; Italiano et al., 2019; Table 1 and Figures 2a, 2b and 9a and Figure S5c in Supporting Information S1). Although the fossil hydrothermal system on ZI evolved into an open fluid system in which crustal, magmatic, and very low atmospheric components mixed (Figures 9a and 11), the geochemical analyses on hydrothermal fluids currently outgassing in the Pontian Archipelago (Figure 2a) show a significant fingerprint

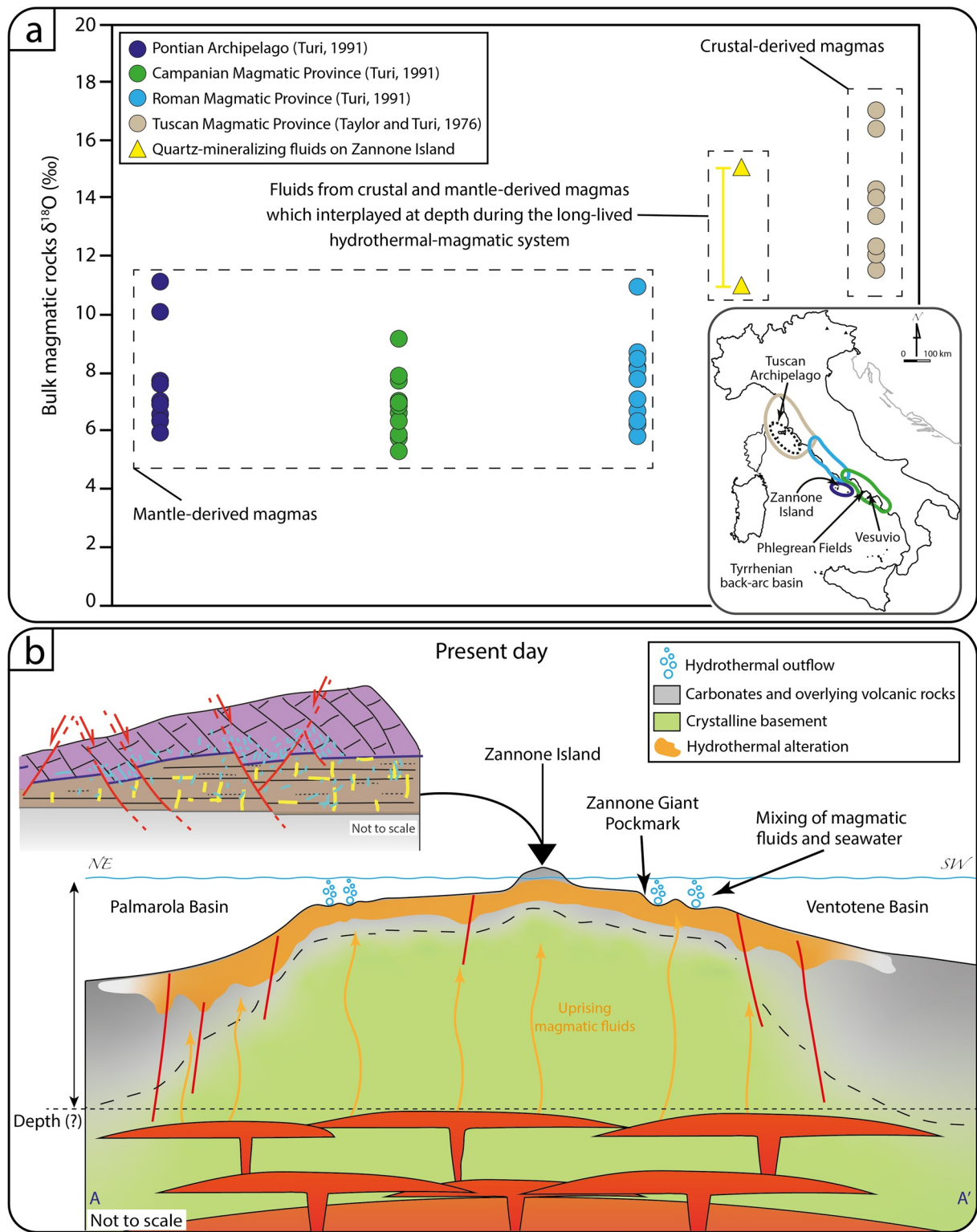


of mantle volatiles with He isotopic ratio up to 3.7 Ra (Italiano et al., 2019; Martorelli et al., 2016; Figure 9a). Hence, we speculate that the Plio-Pleistocene magmatic activity (Cadoux et al., 2005; Peccerillo, 2005), has provided heat and volatiles that fed (and rejuvenated) the long-term hydrothermal system in the Pontian Archipelago (Italiano et al., 2019; Martorelli et al., 2016). Similarly to what was documented in the Colline Metallifere area of the Tuscan region (Bertini et al., 2006; Dini et al., 2008; Villa et al., 2006; Rossetti et al., 2008, 2011; Figure 1a), the fossil-to-active hydrothermal system of the ZI shows a geochemical evolution during the progressive crustal thinning associated with normal faulting and multiple magmatic intrusions related to the long-lived magmatism of the Tyrrhenian back-arc basin. As a whole, the active hydrothermal system of the Pontian Archipelago covers an area of about 60 km<sup>2</sup> (Figure 2a) and its activity is controlled by the back-arc extension (Martorelli et al., 2016). Currently, sulfur springs and hydrothermal vents occur along NE-SW- and NW-SE-striking normal faults and fractures, where fluid-escape morphologies such as cones, mounds, and pockmarks are reported (Italiano et al., 2019; Martorelli et al., 2016; Figures 2a, 2b and 12b). Within the ZGP (Figure 2b), about 2 km to the east of ZI, crusts of native sulfur and altered rocks document sulfur-rich hydrothermal alteration (Conte, Di Bella, et al., 2020) which is similar to what is documented in Ponza and the Pontian Archipelago in general (Figure 2a; Ylagan et al., 1996, 2000). Mixing of hydrothermal fluids with seawater leads to the cooling and neutralization of fluids in an active low-sulfidation hydrothermal system (Conte, Di Bella, et al., 2020; Figure 12b). The widespread occurrence of hydrothermal activity shows that post-volcanism magmatic intrusions are the source of heat and magmatic fluids and actually feed the whole 60 km<sup>2</sup> wide Tyrrhenian back-arc area surrounding ZI (Figure 12b).

There is still an ongoing debate if the magmas involved in the early magmatic stage of the Pontian Archipelago are crustal or mantle-derived. The magmatic products of ZI and the western Pontian Islands were interpreted by Turi et al. (1991) to be crustal-derived magmas related to the Tuscan Magmatic Province, due to their age and high  $\delta^{18}\text{O}$  values  $>\sim 11\text{‰}$ . However, recent petrologic analyses have linked the magmatic products of the whole Pontian Archipelago to the mantle-derived Roman Magmatic Province (Conte, Perinelli, et al., 2020). Our data do not provide a direct answer to this debate that would necessitate a direct study of the magmatic rocks, but allows to put additional constraints to the origin of the fluids. The  $\delta^{18}\text{O}$  values of quartz-mineralizing fluids comprised between  $+11\text{‰}$  and  $+15\text{‰}$  (Figure 8c); suggest a significant contribution of crustal-derived magmas and a likely magmatic affinity with the Tuscan Magmatic Province (e.g., Farina et al., 2018; Taylor & Turi, 1976; Turi et al., 1991) with a minor contribution of mantle-derived magmas (Figure 12a). However, the noble gases in the quartz veins indubitably indicate the presence of a clear mantle-derived component (Figures 9a and 9d). Long lived magmatic-hydrothermal systems are usually sustained by multiple injection of crustal and mantle-derived magmas, as documented in the Tuscan Magmatic Province (Farina et al., 2018; Di Vincenzo et al., 2022 and references therein). Hence, we speculate that different crustal- and mantle-derived magmas could have formed and interplayed depth releasing hydrothermal fluids at different times in the evolution of ZI and Pontian Archipelago (Figure 12). Long-lived magmatic systems in which crustal- and mantle-derived magmas interacted through time have been widely documented both in fossil (e.g., along the Gondwana and Pangea margins; e.g., Cochrane et al., 2014; Wolfram et al., 2019) and active back-arc basins in the Mediterranean region and worldwide (e.g., Tyrrhenian Basin, Peccerillo, 2005; Alboran Basin, Duggen et al., 2004; Okinawa Through, Li et al., 2020).

### 5.9. Insights on the Mode of Hydrothermal Mineralization in the Tyrrhenian Back-Arc

The onshore fossil mineralizations on ZI can be considered as an analog of a very immature stage of back-arc basin formation, when continental crust is presented due to the low amount of crustal stretching. The control of faulting on the generation of hydrothermal mineralizations is clearly indicated by their development along steep vertical faults that interrupted the continuity of impermeable (or low-permeability) horizons, allowing the mixing between magmatic and meteoric fluids (and not with downward percolating seawater, as in Kuroko-type processes; Ohmoto, 1996) and the deposition of high-temperature (monazite, rutile, and chalcopyrite) to low temperature (barite and neo-formed smectite and pyrite) ore deposits. The active mineralizations in the ZGP, where sulfide deposits derive from mixing of hydrothermal fluids with seawater (Conte, Di Bella, et al., 2020) can be instead considered as an analog of more mature (but still immature), in the definition of Fouquet et al. (1993) submarine back-arc conditions, produced by more extensive crustal stretching.



**Figure 12.** (a) Oxygen isotope composition of magmatic rocks from Roman, Campanian and Tuscan Magmatic Provinces and quartz-mineralizing fluids. (b) Schematic section showing the structural high where Zannone Island relies on, and that separates the Pliocene-Quaternary Palmarola (to the NW) and Ventotene (to the SE) Basins. The intrusions which feed the active hydrothermal system in the area, the hydrothermal outflow close to Zannone Island, and the hydrothermal alteration area on the seabottom and in subsurface area are also shown. The trace of the schematic section is shown in Figure 2a.



## 6. Conclusions

The ZI represents an ideal locality to study the structural control, composition, and evolution of a long-lived hydrothermal system in the back-arc of the central Apennine orogen. The adopted multidisciplinary approach allowed us to draw the *P-T-X* and rheological evolution of the hydrothermal system:

1. Hydrothermal activity is associated with extensional tectonics, which began during the late Messinian-early Pliocene time.
2. A magmatic origin is inferred for the early stage hydrothermal fluids responsible for the syn-tectonic quartz veining.
3. The secondary permeability distribution associated with normal faulting and fracturing modulated and assisted fluid flow, promoting mixing of magmatic and meteoric fluids and the interaction with carbonate rocks. Progressive mixing and interaction with carbonate rocks led to the cooling of the fluid(s) and pH increase leading to carbonate precipitation.
4. The late stage of carbonate mineralization occurred at shallower depth, when normal fault activity enhanced the downwelling of meteoric fluids, causing changes in geochemical and *P-T* conditions of the hydrothermal system.
5. The fossil-to-active hydrothermal history of the area of ZI is associated with a polyphase and long-lived magmatic activity in which different crustal and mantle-derived magmas interplayed at depth.
6. The hydrothermal mineralizations on ZI can be considered as an archive for the mode through which crustal thinning operated in space and time during formation of the Tyrrhenian back-arc domain.

## Data Availability Statement

Analytical data are available in Supporting Information S1 and in the Figshare external repository <https://doi.org/10.6084/m9.figshare.19550398>.

## Acknowledgments

This work has been funded by Progetto di Ateneo Sapienza 2019 and 2021 (E. Carminati) and 2020 (L. Aldega) and Bando per il finanziamento di progetti di ricerca congiunti per la mobilità all'estero di studenti di dottorato (M. Curzi and S. Franchini). The Editor, an anonymous reviewer and Prof. L. Jolivet are thanked for comments and revisions. Geological field work on Zannone Island was performed together with L. Cardello and L. Smeraglia, who the authors thank. The authors thank M. Jaggi and S. Franchini for assistance with clumped isotope analyses, I. Baneschi for assistance with O isotope analyses on quartz veins, M. Albano for assistance with scanning electron microscopy analysis, and D. Mannelta for preparation of thin sections. The authors thank M. Misseri, M. Tantiolo, and Ygor Oliveri for helping in sample preparation and in the isotope analysis of noble gases and carbon isotopes of CO<sub>2</sub> carried out in the laboratories of INGV-Palermo.

## References

- Acocella, V., & Funicello, R. (2006). Transverse systems along the extensional Tyrrhenian margin of central Italy and their influence on volcanism. *Tectonics*, 25(2), TC2003. <https://doi.org/10.1029/2005tc001845>
- Anderson, N. T., Kelson, J. R., Kele, S., Daëron, M., Bonifacie, M., Horita, J., et al. (2021). A unified clumped isotope thermometer calibration (0.5–1, 100 °C) using carbonate-based standardization. *Geophysical Research Letters*, 48(7), e2020GL092069. <https://doi.org/10.1029/2020gl092069>
- Ballentine, C. J., Burgess, R., & Marty, B. (2002). Tracing fluid origin, transport and interaction in the crust. *Reviews in Mineralogy and Geochemistry*, 47(1), 539–614. <https://doi.org/10.2138/rmg.2002.47.13>
- Bendel, V., Fouquet, Y., Auzende, J. M., Lagabrielle, Y., Grimaud, D., & Urabe, T. (1993). The White Lady hydrothermal field, North Fiji back-arc basin, southwest Pacific. *Economic Geology*, 88(8), 2237–2245. <https://doi.org/10.2113/gsecongeo.88.8.2237>
- Bertini, G., Casini, M., Gianelli, G., & Pandeli, E. (2006). Geological structure of a long-living geothermal system, Larderello, Italy. *Terra Nova*, 18(3), 163–169. <https://doi.org/10.1111/j.1365-3121.2006.00676.x>
- Billi, A., & Tiberti, M. M. (2009). Possible causes of arc development in the Apennines, central Italy. *The Geological Society of America Bulletin*, 121(9–10), 1409–1420. <https://doi.org/10.1130/b26335.1>
- Binns, R. A., & Scott, S. D. (1993). Actively forming polymetallic sulfide deposits associated with felsic volcanic rocks in the eastern Manus back-arc basin, Papua New Guinea. *Economic Geology*, 88(8), 2226–2236. <https://doi.org/10.2113/gsecongeo.88.8.2226>
- Broggi, A. (2004). Faults linkage, damage rocks and hydrothermal fluid circulation: Tectonic interpretation of the Rapolano Terme travertines (southern Tuscany, Italy) in the context of Northern Apennines Neogene-Quaternary extension. *Eclogae Geologicae Helveticae*, 97(3), 307–320. <https://doi.org/10.1007/s00015-004-1134-5>
- Broggi, A., Fabbrini, L., & Liotta, D. (2011). Sb–Hg ore deposit distribution controlled by brittle structures: The case of the Selvena mining district (Monte Amiata, Tuscany, Italy). *Ore Geology Reviews*, 41(1), 35–48. <https://doi.org/10.1016/j.oregeorev.2011.06.004>
- Broggi, A., & Fulignati, P. (2012). Tectonic control on hydrothermal circulation and fluid evolution in the Pietratonda–Poggio Peloso (southern Tuscany, Italy) carbonate-hosted Sb-mineralization. *Ore Geology Reviews*, 44, 158–171. <https://doi.org/10.1016/j.oregeorev.2011.11.003>
- Broggi, A., Liotta, D., Capezzuoli, E., Matera, P. F., Kele, S., Soligo, M., et al. (2020). Travertine deposits constraining transfer zone neotectonics in geothermal areas: An example from the inner Northern Apennines (Bagno Vignoni-Val d'Orcia area, Italy). *Geothermics*, 85, 101763. <https://doi.org/10.1016/j.geothermics.2019.101763>
- Burnard, P. G., Hu, R. Z., Turner, G., & Bi, X. W. (1999). Mantle, crustal and atmospheric noble gases in Ailaoshan gold deposits, Yunnan Province, China. *Geochimica et Cosmochimica Acta*, 63(10), 1595–1604. [https://doi.org/10.1016/s0016-7037\(99\)00108-8](https://doi.org/10.1016/s0016-7037(99)00108-8)
- Cadoux, A., Pinti, D. L., Aznar, C., Chiesa, S., & Gillot, P. Y. (2005). New chronological and geochemical constraints on the genesis and geological evolution of Ponza and Palmarola volcanic islands (Tyrrhenian Sea, Italy). *Lithos*, 81(1–4), 121–151. <https://doi.org/10.1016/j.lithos.2004.09.020>
- Caracausi, A., Nicolosi, M., Nuccio, P. M., Favara, R., Paternoster, M., & Rosciglione, A. (2013). Geochemical insight into differences in the physical structures and dynamics of two adjacent maar lakes at Mt. Vulture volcano (southern Italy). *Geochemistry, Geophysics, Geosystems*, 14(5), 1411–1434. <https://doi.org/10.1002/ggge.20111>
- Caracausi, A., & Paternoster, M. (2015). Radiogenic helium degassing and rock fracturing: A case study of the southern Apennines active tectonic region. *Journal of Geophysical Research: Solid Earth*, 120(4), 2200–2211. <https://doi.org/10.1002/2014jb011462>

- Caracausi, A., Paternoster, M., & Nuccio, P. M. (2015). Mantle CO<sub>2</sub> degassing at Mt. Vulture volcano (Italy): Relationship between CO<sub>2</sub> outgassing of volcanoes and the time of their last eruption. *Earth and Planetary Science Letters*, 411, 268–280. <https://doi.org/10.1016/j.epsl.2014.11.049>
- Carminati, E., Lustrino, M., Cuffaro, M., & Doglioni, C. (2010). Tectonics, magmatism and geodynamics of Italy: What we know and what we imagine. *Journal of the Virtual Explorer*, 36(8), 10–3809. <https://doi.org/10.3809/jvirtex.2010.00226>
- Cavinato, G. P., & Celles, P. D. (1999). Extensional basins in the tectonically bimodal central Apennines fold-thrust belt, Italy: Response to corner flow above a subducting slab in retrograde motion. *Geology*, 27(10), 955–958. [https://doi.org/10.1130/0091-7613\(1999\)027<0955:ebittb>2.3.co;2](https://doi.org/10.1130/0091-7613(1999)027<0955:ebittb>2.3.co;2)
- Chiocci, F. L., & Orlando, L. (1996). Lowstand terraces on Tyrrhenian Sea steep continental slopes. *Marine Geology*, 134(1–2), 127–143. [https://doi.org/10.1016/0025-3227\(96\)00023-0](https://doi.org/10.1016/0025-3227(96)00023-0)
- Chiodini, G., Caliro, S., Cardellini, C., Granieri, D., Avino, R., Baldini, A., et al. (2010). Long-term variations of the Campi Flegrei, Italy, volcanic system as revealed by the monitoring of hydrothermal activity. *Journal of Geophysical Research*, 115(B3), B03205. <https://doi.org/10.1029/2008jb006258>
- Clayton, R. N., O'Neil, J. R., & Mayeda, T. K. (1972). Oxygen isotope exchange between quartz and water. *Journal of Geophysical Research*, 77(17), 3057–3067. <https://doi.org/10.1029/jb077i017p03057>
- Cochrane, R., Spikings, R., Gerdes, A., Ulianov, A., Mora, A., Villagómez, D., et al. (2014). Permo-Triassic anatexis, continental rifting and the disassembly of western Pangaea. *Lithos*, 190, 383–402. <https://doi.org/10.1016/j.lithos.2013.12.020>
- Conte, A. M., Di Bella, L., Ingrassia, M., Perinelli, C., & Martorelli, E. (2020). Alteration and mineralization products of the Zannone Giant Pockmark (Zannone hydrothermal field, central Tyrrhenian Sea). *Minerals*, 10(7), 581. <https://doi.org/10.3390/min10070581>
- Conte, A. M., Perinelli, C., Bosman, A., Castorina, F., Conti, A., Cuffaro, M., et al. (2020). Tectonics, dynamics, and Plio-Pleistocene magmatism in the central Tyrrhenian Sea: Insights from the submarine transitional basalts of the Ventotene volcanic ridge (Pontine Islands, Italy). *Geochemistry, Geophysics, Geosystems*, 21(12), e2020GC009346. <https://doi.org/10.1029/2020gc009346>
- Corsini, F., Cortecci, G., Leone, G., & Tanelli, G. (1980). Sulfur isotope study of the skarn-(Cu-Pb-zn) sulfide deposit of Valle del Temperino, Campiglia Marittima, Tuscany, Italy. *Economic Geology*, 75(1), 83–96. <https://doi.org/10.2113/gsecongeo.75.1.83>
- Cortecci, G., Lattanzi, P., & Tanelli, G. (1985). C-and O-isotope and fluid inclusion studies of carbonates from pyrite and polymetallic ore deposits and associated country rocks (southern Tuscany, Italy). *Chemical Geology: Isotope Geoscience section*, 58(1–2), 121–128. [https://doi.org/10.1016/0168-9622\(85\)90032-6](https://doi.org/10.1016/0168-9622(85)90032-6)
- Cosentino, D., Cipollari, P., Marsili, P., & Scrocca, D. (2010). Geology of the central Apennines: A regional review. *Journal of the Virtual Explorer*, 36(11), 1–37. <https://doi.org/10.3809/jvirtex.2010.00223>
- Cuffaro, M., Martorelli, E., Bosman, A., Conti, A., Bigi, S., Muccini, F., et al. (2016). The Ventotene volcanic ridge: A newly explored complex in the central Tyrrhenian Sea (Italy). *Bulletin of Volcanology*, 78(12), 86. <https://doi.org/10.1007/s00445-016-1081-9>
- Curzi, M., Billi, A., Carminati, E., Rossetti, F., Roper, R. A., Aldega, L., et al. (2020). Disproving the presence of Paleozoic-Triassic metamorphic rocks on the Island of Zannone (central Italy): Implications for the early stages of the Tyrrhenian-Apennines tectonic evolution. *Tectonics*, 39(12), e2020TC006296. <https://doi.org/10.1029/2020tc006296>
- Dekov, V. M., & Savelli, C. (2004). Hydrothermal activity in the SE Tyrrhenian Sea: An overview of 30 years of research. *Marine Geology*, 204(1–2), 161–185. [https://doi.org/10.1016/s0025-3227\(03\)00355-4](https://doi.org/10.1016/s0025-3227(03)00355-4)
- De Rita, D., Funicello, R., Pantosti, D., Salvini, F., & Sposato, A. (1986). Geological and structural characteristics of the Pontine Islands (Italy) and implications with the evolution of the Tyrrhenian margin. *Memorie della Società Geologica Italiana*, 36, 55–65.
- Diaferia, G., Cammarano, F., & Faccenna, C. (2019). Thermal structure of a vanishing subduction system: An example of seismically-derived crustal temperature along the Italian peninsula. *Geophysical Journal International*, 219(1), 239–247. <https://doi.org/10.1093/gji/ggz289>
- Dini, A. (2003). Ore deposits, industrial minerals and geothermal resources. *Periodico di Mineralogia*, 72(2), 41–52.
- Dini, A., Mazzarini, F., Musumeci, G., & Rocchi, S. (2008). Multiple hydro-fracturing by boron-rich fluids in the Late Miocene contact aureole of eastern Elba Island (Tuscany, Italy). *Terra Nova*, 20(4), 318–326. <https://doi.org/10.1111/j.1365-3121.2008.00823.x>
- Di Vincenzo, G., Vezzoni, S., Dini, A., & Rocchi, S. (2022). Timescale of a magmatic-hydrothermal system revealed by <sup>40</sup>Ar–<sup>39</sup>Ar geochronology: The Mio-Pliocene Campiglia Marittima system (Tuscany, Italy). *Scientific Reports*, 12(1), 1–13. <https://doi.org/10.1038/s41598-022-10867-9>
- Duggen, S., Hoernle, K., van den Bogaard, P., & Harris, C. (2004). Magmatic evolution of the Alboran region: The role of subduction in forming the western Mediterranean and causing the Messinian Salinity Crisis. *Earth and Planetary Science Letters*, 218(1–2), 91–108. [https://doi.org/10.1016/s0012-821x\(03\)00632-0](https://doi.org/10.1016/s0012-821x(03)00632-0)
- Faccenna, C., Becker, T. W., Lucente, F. P., Jolivet, L., & Rossetti, F. (2001). History of subduction and back arc extension in the Central Mediterranean. *Geophysical Journal International*, 145(3), 809–820. <https://doi.org/10.1046/j.0956-540x.2001.01435.x>
- Farina, F., Dini, A., Davies, J. H., Ovtcharova, M., Greber, N. D., Bouvier, A. S., et al. (2018). Zircon petrochronology reveals the timescale and mechanism of anatectic magma formation. *Earth and Planetary Science Letters*, 495, 213–223. <https://doi.org/10.1016/j.epsl.2018.05.021>
- Fouquet, Y., Charlou, J. L., von Stackelberg, U., Wiedicke, M., Erzinger, J., Herzig, P. M., & Muehe, R. (1993). Metallogenesis in back-arc environments: The Lau Basin example. *Economic Geology*, 88(8), 2154–2181. <https://doi.org/10.2113/gsecongeo.88.8.2154>
- Fouquet, Y., Stackelberg, U. V., Charlou, J. L., Donval, J. P., Erzinger, J., Foucher, J. P., et al. (1991). Hydrothermal activity and metallogenesis in the Lau back-arc basin. *Nature*, 349(6312), 778–781. <https://doi.org/10.1038/349778a0>
- Frey, M. (1987). The reaction-isograd kaolinite + quartz = pyrophyllite + H<sub>2</sub>O, Helvetic Alps, Switzerland. *Schweizerische Mineralogische und Petrographische Mitteilungen*, 67(1), 1–11.
- Fulignati, P. (2018). Hydrothermal fluid evolution in the 'Botro ai Marmi' quartz-monzonitic intrusion, Campiglia Marittima, Tuscany, Italy. Evidence from a fluid-inclusion investigation. *Mineralogical Magazine*, 82(5), 1169–1185. <https://doi.org/10.1180/mgm.2018.116>
- Gautheron, C., Moreira, M., & Allègre, C. (2005). He, Ne and Ar composition of the European lithospheric mantle. *Chemical Geology*, 217(1–2), 97–112. <https://doi.org/10.1016/j.chemgeo.2004.12.009>
- Gennaro, M. E., Grassa, F., Martelli, M., Renzulli, A., & Rizzo, A. L. (2017). Carbon isotope composition of CO<sub>2</sub>-rich inclusions in cumulate-forming mantle minerals from Stromboli volcano (Italy). *Journal of Volcanology and Geothermal Research*, 346, 95–103. <https://doi.org/10.1016/j.jvolgeores.2017.04.001>
- Giggenbach, W. F. (1997). Relative importance of thermodynamic and kinetic processes in governing the chemical and isotopic composition of carbon gases in high-heatflow sedimentary basins. *Geochimica et Cosmochimica Acta*, 61(17), 3763–3785. [https://doi.org/10.1016/s0016-7037\(97\)00171-3](https://doi.org/10.1016/s0016-7037(97)00171-3)
- Goodwin, N. R., Burgess, R., Craw, D., Teagle, D. A., & Ballentine, C. J. (2017). Noble gases fingerprint a metasedimentary fluid source in the Macraes orogenic gold deposit, New Zealand. *Mineralium Deposita*, 52(2), 197–209. <https://doi.org/10.1007/s00126-016-0648-x>
- Graham, D. W. (2002). Noble gas isotope geochemistry of mid-ocean ridge and ocean island basalts: Characterization of mantle source reservoirs. *Reviews in Mineralogy and Geochemistry*, 47(1), 247–319. <https://doi.org/10.2138/rmg.2002.47.8>



- Graupner, T., Niedermann, S., Kempe, U., Klemd, R., & Bechtel, A. (2006). Origin of ore fluids in the Muruntau gold system: Constraints from noble gas, carbon isotope and halogen data. *Geochimica et Cosmochimica Acta*, 70(21), 5356–5370. <https://doi.org/10.1016/j.gca.2006.08.013>
- Halbach, P., Nakamura, K. I., Wahsner, M., Lange, J., Sakai, H., Käselitz, L., et al. (1989). Probable modern analogue of Kuroko-type massive sulphide deposits in the Okinawa Trough back-arc basin. *Nature*, 338(6215), 496–499. <https://doi.org/10.1038/338496a0>
- Hemley, J. J., & Hunt, J. P. (1992). Hydrothermal ore-forming processes in the light of studies in rock-buffered systems; II. Some general geologic applications. *Economic Geology*, 87(1), 23–43. <https://doi.org/10.2113/gsecongeo.87.1.23>
- Hilgers, C., & Urai, J. L. (2002). Microstructural observations on natural syntectonic fibrous veins: Implications for the growth process. *Tectonophysics*, 352(3–4), 257–274. [https://doi.org/10.1016/s0040-1951\(02\)00185-3](https://doi.org/10.1016/s0040-1951(02)00185-3)
- Hu, R. Z., Burnard, P. G., Bi, X. W., Zhou, M. F., Peng, J. T., Su, W. C., & Zhao, J. H. (2009). Mantle-derived gaseous components in ore-forming fluids of the Xiangshan uranium deposit, Jiangxi Province, China: Evidence from He, Ar and C isotopes. *Chemical Geology*, 266(1–2), 86–95. <https://doi.org/10.1016/j.chemgeo.2008.07.017>
- Ingrassia, M., Martorelli, E., Bosman, A., Macelloni, L., Sposato, A., & Chiocci, F. L. (2015). The Zannone Giant Pockmark: First evidence of a giant complex seeping structure in shallow-water, central Mediterranean Sea, Italy. *Marine Geology*, 363, 38–51. <https://doi.org/10.1016/j.margeo.2015.02.005>
- Inoue, A. (1995). Formation of clay minerals in hydrothermal environments. In *Origin and mineralogy of clays* (pp. 268–329). Springer.
- Ishibashi, J. I., Ikegami, F., Tsuji, T., & Urabe, T. (2015). Hydrothermal activity in the Okinawa Trough back-arc basin: Geological background and hydrothermal mineralization. In *Subseafloor biosphere linked to hydrothermal systems* (pp. 337–359). Springer.
- Italiano, F., De Santis, A., Favali, P., Rainone, M. L., Rusi, S., & Signanini, P. (2014). The Marsili volcanic seamount (southern Tyrrhenian Sea): A potential offshore geothermal resource. *Energies*, 7(7), 4068–4086. <https://doi.org/10.3390/en7074068>
- Italiano, F., Romano, D., Caruso, C., Longo, M., Corbo, A., & Lazzaro, G. (2019). Magmatic signature in submarine hydrothermal fluids vented offshore Ventotene and Zannone Islands (Pontine Archipelago, central Italy). *Geofluids*, 2019, 8759609. <https://doi.org/10.1155/2019/8759609>
- Jolivet, L., Faccenna, C., Goffé, B., Mattei, M., Rossetti, F., Brunet, C., et al. (1998). Midcrustal shear zones in postorogenic extension: Example from the northern Tyrrhenian Sea. *Journal of Geophysical Research*, 103(B6), 12123–12160. <https://doi.org/10.1029/97jb03616>
- Kendrick, M. A., & Burnard, P. (2013). Noble gases and halogens in fluid inclusions: A journey through the Earth's crust. In *The noble gases as geochemical tracers* (pp. 319–369). Springer.
- Kendrick, M. A., Honda, M., Oliver, N. H. S., & Phillips, D. (2011). The noble gas systematics of late-orogenic H<sub>2</sub>O–CO<sub>2</sub> fluids, Mt Isa, Australia. *Geochimica et Cosmochimica Acta*, 75(6), 1428–1450. <https://doi.org/10.1016/j.gca.2010.12.005>
- Larsson, D. (2001). Transition of granite to quartz-kyanite rock at Hålsjöberg, southern Sweden: Consequence of acid leaching and later metamorphism. *Gff*, 123(4), 237–246. <https://doi.org/10.1080/11035890101234237>
- Lee, J.-Y., Marti, K., Severinghaus, J. P., Kawamura, K., Yoo, H.-S., Lee, J. B., & Kim, J. S. (2006). A redetermination of the isotopic abundances of atmospheric Ar. *Geochimica et Cosmochimica Acta*, 70(17), 4507–4512. <https://doi.org/10.1016/j.gca.2006.06.1563>
- Li, L., & Ji, S. (2021). A new interpretation for formation of orthogonal joints in quartz sandstone. *Journal of Rock Mechanics and Geotechnical Engineering*, 13(2), 289–299. <https://doi.org/10.1016/j.jrmge.2020.08.003>
- Li, X., Zeng, Z., Dan, W., Yang, H., Wang, X., Fang, B., & Li, Q. (2020). Source lithology and crustal assimilation recorded in low δ<sup>18</sup>O olivine from Okinawa Trough, back-arc basin. *Lithos*, 360, 105444. <https://doi.org/10.1016/j.lithos.2020.105444>
- Liotta, D., Ruggieri, G., Brogi, A., Fulignati, P., Dini, A., & Nardini, I. (2010). Migration of geothermal fluids in extensional terrains: The ore deposits of the Boccheggiano-Montieri area (southern Tuscany, Italy). *International Journal of Earth Sciences*, 99(3), 623–644. <https://doi.org/10.1007/s00531-008-0411-3>
- Malinverno, A., & Ryan, W. B. (1986). Extension in the Tyrrhenian Sea and shortening in the Apennines as result of arc migration driven by sinking of the lithosphere. *Tectonics*, 5(2), 227–245. <https://doi.org/10.1029/tc005i002p00227>
- Marani, M. P., Gamberi, F., & Savelli, C. (1997). Shallow-water polymetallic sulfide deposits in the Aeolian island arc. *Geology*, 25(9), 815–818. [https://doi.org/10.1130/0091-7613\(1997\)025<0815:swpsdi>2.3.co;2](https://doi.org/10.1130/0091-7613(1997)025<0815:swpsdi>2.3.co;2)
- Martarelli, L., Ferrini, V., & Masi, U. (1995). Trace-element evidence for the genesis of the pyrite vein deposit of Campiano (southern Tuscany, Italy). *Periodico di Mineralogia*, 64, 349–366.
- Martelli, M., Nuccio, P. M., Stuart, F. M., Burgess, R., Ellam, R. M., & Italiano, F. (2004). Helium–strontium isotope constraints on mantle evolution beneath the Roman Comagmatic Province, Italy. *Earth and Planetary Science Letters*, 224(3–4), 295–308. <https://doi.org/10.1016/j.epsl.2004.05.025>
- Martorelli, E., Italiano, F., Ingrassia, M., Macelloni, L., Bosman, A., Conte, A. M., et al. (2016). Evidence of a shallow water submarine hydrothermal field off Zannone Island from morphological and geochemical characterization: Implications for Tyrrhenian Sea Quaternary volcanism. *Journal of Geophysical Research: Solid Earth*, 121(12), 8396–8414. <https://doi.org/10.1002/2016jb013103>
- Merlini, S., & Mostardini, F. (1986). Appennino centro-meridionale: Sesioni geologiche e proposta di modello strutturale. In *Geologia dell'Italia centrale* (Vol. 73, pp. 147–149). Congresso nazionale.
- Metric, N., Santacroce, R., & Savelli, C. (1988). Ventotene, a potassic quaternary volcano in central Tyrrhenian Sea. *Rendiconti della Società Italiana di Mineralogia e Petrologia*, 43, 1195–1213.
- Minissale, A., Magro, G., Martinelli, G., Vaselli, O., & Tassi, G. F. (2000). Fluid geochemical transect in the Northern Apennines (central-northern Italy): Fluid genesis and migration and tectonic implications. *Tectonophysics*, 319(3), 199–222. [https://doi.org/10.1016/s0040-1951\(00\)00031-7](https://doi.org/10.1016/s0040-1951(00)00031-7)
- Minissale, A., Magro, G., Vaselli, O., Verrucchi, C., & Perticone, I. (1997). Geochemistry of water and gas discharges from the Mt. Amiata silicic complex and surrounding areas (central Italy). *Journal of Volcanology and Geothermal Research*, 79(3–4), 223–251. [https://doi.org/10.1016/s0377-0273\(97\)00028-0](https://doi.org/10.1016/s0377-0273(97)00028-0)
- Mort, K., & Woodcock, N. H. (2008). Quantifying fault breccia geometry: Dent fault, NW England. *Journal of Structural Geology*, 30(6), 701–709. <https://doi.org/10.1016/j.jsg.2008.02.005>
- Ohmoto, H. (1996). formation of volcanogenic massive sulfide deposits: The Kuroko perspective. *Ore Geology Reviews*, 10(3–6), 135–177. [https://doi.org/10.1016/0169-1368\(95\)00021-6](https://doi.org/10.1016/0169-1368(95)00021-6)
- Ozima, M., & Podosek, F. A. (2002). *Noble gas geochemistry* (pp. 1–286). Cambridge University Press.
- Pantosti, D., & Velonà, M. (1986). Tettonica recente nell'Isola di Zannone e nella piattaforma circostante (Arcipelago Pontino, Italia Centrale). *Memorie della Società Geologica Italiana*, 35, 623–629.
- Paoli, G., Dini, A., Petrelli, M., & Rocchi, S. (2019). HFSE-REE transfer mechanisms during Metasomatism of a Late Miocene Peraluminous granite Intruding a carbonate host (Campiglia Marittima, Tuscany). *Minerals*, 9(11), 682. <https://doi.org/10.3390/min9110682>
- Parotto, M., & Praturlon, A. (1975). Geological summary of central Apennines. *Quaderni della Ricerca Scientifica*, 90, 257–311.
- Patacca, E., Sartori, R., & Scandone, P. (1990). Tyrrhenian basin and Apenninic arcs: Kinematic relations since late Tortonian times. *Memorie della Società Geologica Italiana*, 45, 425–451.
- Patacca, E., & Scandone, P. (2007). Geology of the southern Apennines. *Bollettino della Società Geologica Italiana*, 7, 75–119.

- Peccerillo, A. (2005). *Plio-Quaternary volcanism in Italy* (Vol. 365). Springer-Verlag Berlin Heidelberg.
- Rabiee, A., Rossetti, F., Tecce, F., Asahara, Y., Azizi, H., Glodny, J., et al. (2019). Multiphase magma intrusion, ore-enhancement and hydrothermal carbonatization in the Siah-Kamar porphyry Mo deposit, Urumieh-Dokhtar magmatic zone, NW Iran. *Ore Geology Reviews*, *110*, 102930. <https://doi.org/10.1016/j.oregeorev.2019.05.016>
- Reyes, A. G. (1990). Petrology of Philippine geothermal systems and the application of alteration mineralogy to their assessment. *Journal of Volcanology and Geothermal Research*, *43*(1–4), 279–309. [https://doi.org/10.1016/0377-0273\(90\)90057-m](https://doi.org/10.1016/0377-0273(90)90057-m)
- Reyes, A. G., Grapes, R., & Clemente, V. C. (2003). Fluid-rock interaction at the magmatic-hydrothermal interface of the Mount Cagua geothermal system, Philippines. *Special Publication-Society of Economic Geologists*, *10*, 197–222. <https://doi.org/10.5382/SP.10.12>
- Rossetti, F., Aldega, L., Tecce, F., Balsamo, F., Billi, A., & Brilli, M. (2011). Fluid flow within the damage zone of the Boccheggiano extensional fault (Larderello–Travale geothermal field, central Italy): Structures, alteration and implications for hydrothermal mineralization in extensional settings. *Geological Magazine*, *148*(4), 558–579. <https://doi.org/10.1017/s001675681000097x>
- Rossetti, F., Balsamo, F., Villa, I. M., Bouybaouenne, M., Faccenna, C., & Funiello, R. (2008). Pliocene–Pleistocene HT–LP metamorphism during multiple granitic intrusions in the southern branch of the Larderello geothermal field (southern Tuscany, Italy). *Journal of the Geological Society*, *165*(1), 247–262. <https://doi.org/10.1144/0016-76492006-132>
- Sano, Y., & Marty, B. (1995). Origin of carbon in fumarolic gas from island arcs. *Chemical Geology*, *119*(1–4), 265–274. [https://doi.org/10.1016/0009-2541\(94\)00097-r](https://doi.org/10.1016/0009-2541(94)00097-r)
- Sano, Y., & Wakita, H. (1985). Geographical distribution of  $^3\text{He}/^4\text{He}$  ratios in Japan: Implications for arc tectonics and incipient magmatism. *Journal of Geophysical Research*, *90*(B10), 8729–8741. <https://doi.org/10.1029/jb090ib10p08729>
- Segre, A. G. (1954). Morfologia e geologia. In E. Zavattari, et al. (Eds.), *Biogeografia dell'Isola di Zannone, Rendiconti Accademia Nazionale dei XL* (s. 4, 4-5, 7).
- Silverstone, J., Axen, G. J., & Luther, A. (2012). Fault localization controlled by fluid infiltration into mylonites: Formation and strength of low-angle normal faults in the midcrustal brittle-plastic transition. *Journal of Geophysical Research*, *117*(B6), B06210. <https://doi.org/10.1029/2012jb009171>
- Serri, G., Innocenti, F., & Manetti, P. (1993). Geochemical and petrological evidence of the subduction of delaminated Adriatic continental lithosphere in the genesis of the Neogene-Quaternary magmatism of central Italy. *Tectonophysics*, *223*(1–2), 117–147. [https://doi.org/10.1016/0040-1951\(93\)90161-c](https://doi.org/10.1016/0040-1951(93)90161-c)
- Shen, Z., Yu, B., Bai, C., Han, S., & Liu, H. (2020). Origin of bedding-parallel calcite veins from lacustrine shale in the Eocene Dongying depression, Bohai Bay basin, China. *Geofluids*, *2020*, 1–23. <https://doi.org/10.1155/2020/8883297>
- Shuster, D. L., & Farley, K. A. (2005). Diffusion kinetics of proton-induced  $^{21}\text{Ne}$ ,  $^3\text{He}$ , and  $^4\text{He}$  in quartz. *Geochimica et Cosmochimica Acta*, *69*(9), 2349–2359. <https://doi.org/10.1016/j.gca.2004.11.002>
- Sibson, R. H. (2000). Fluid involvement in normal faulting. *Journal of Geodynamics*, *29*(3–5), 469–499. [https://doi.org/10.1016/s0264-3707\(99\)00042-3](https://doi.org/10.1016/s0264-3707(99)00042-3)
- Sibson, R. H., & Rowland, J. V. (2003). Stress, fluid pressure and structural permeability in seismogenic crust, North Island, New Zealand. *Geophysical Journal International*, *154*(2), 584–594. <https://doi.org/10.1046/j.1365-246x.2003.01965.x>
- Stuart, F. M., Burnard, P. G., Taylor, R. P., & Turner, G. (1995). Resolving mantle and crustal contributions to ancient hydrothermal fluids: He–Ar isotopes in fluid inclusions from Dae Hwa W–Mo mineralisation, South Korea. *Geochimica et Cosmochimica Acta*, *59*(22), 4663–4673. [https://doi.org/10.1016/0016-7037\(95\)00300-2](https://doi.org/10.1016/0016-7037(95)00300-2)
- Stuart, F. M., & Turner, G. (1992). The abundance and isotopic composition of the noble gases in ancient fluids. *Chemical Geology: Isotope Geoscience section*, *101*(1–2), 97–109. [https://doi.org/10.1016/0009-2541\(92\)90207-1](https://doi.org/10.1016/0009-2541(92)90207-1)
- Stuart, F. M., Turner, G., Duckworth, R. C., & Fallick, A. E. (1994). Helium-isotopes as tracers of trapped hydrothermal fluids in ocean-floor sulphides. *Geology*, *22*(9), 823–826. [https://doi.org/10.1130/0091-7613\(1994\)022<0823:hiatot>2.3.co;2](https://doi.org/10.1130/0091-7613(1994)022<0823:hiatot>2.3.co;2)
- Tang, Y., Bi, X., Fayek, M., Stuart, F. M., Wu, L., Jiang, G., et al. (2017). Genesis of the Jinding Zn–Pb deposit, northwest Yunnan Province, China: Constraints from rare Earth elements and noble gas isotopes. *Ore Geology Reviews*, *90*, 970–986. <https://doi.org/10.1016/j.oregeorev.2017.04.024>
- Tavani, S., Cardello, G. L., Vignaroli, G., Balsamo, F., Parente, M., Sabbatino, M., et al. (2021). Segmentation of the Apenninic margin of Tyrrhenian back-arc basin forced by the subduction of an inherited transform system. *Tectonics*, *40*(9), e2021TC006770. <https://doi.org/10.1029/2021TC006770>
- Taylor, H. P., & Turi, B. (1976). High- $^{18}\text{O}$  igneous rocks from the Tuscan magmatic province, Italy. *Contributions to Mineralogy and Petrology*, *55*(1), 33–54. <https://doi.org/10.1007/bf00372753>
- Tricoli, G. (1855). *Monografia per le isole del gruppo Ponziaco*. Stamp. Marcellino.
- Turi, B., Taylor, H. P., Jr., & Ferrara, G. (1991). Comparisons of  $^{18}\text{O}/^{16}\text{O}$  and  $^{87}\text{Sr}/^{86}\text{Sr}$  in volcanic rocks from the Pontine Islands, M. Ernici, and Campania with other areas in Italy. *Special Publication – Geochemical Society*, *3*, 307–324.
- Vignaroli, G., Aldega, L., Balsamo, F., Billi, A., De Benedetti, A. A., De Filippis, L., et al. (2015). A way to hydrothermal paroxysm, Colli Albano Volcano, Italy. *The Geological Society of America Bulletin*, *127*(5–6), 672–687. <https://doi.org/10.1130/b31139.1>
- Vignaroli, G., Berardi, G., Billi, A., Kele, S., Rossetti, F., Soligo, M., & Bernasconi, S. M. (2016). Tectonics, hydrothermalism, and paleoclimate recorded by Quaternary travertines and their spatio-temporal distribution in the Albegna basin, central Italy: Insights on Tyrrhenian margin neotectonics. *Lithosphere*, *8*(4), 335–358. <https://doi.org/10.1130/1507.1>
- Villa, I. M., Ruggieri, G., Puxeddu, M., & Bertini, G. (2006). Geochronology and isotope transport systematics in a subsurface granite from the Larderello–Travale geothermal system (Italy). *Journal of Volcanology and Geothermal Research*, *152*(1–2), 20–50. <https://doi.org/10.1016/j.jvolgeores.2005.09.011>
- Wolfram, L. C., Weinberg, R. F., Nebel, O., Hamza, K., Hasalová, P., Míková, J., & Becchio, R. (2019). A 60-Myr record of continental back-arc differentiation through cyclic melting. *Nature Geoscience*, *12*(3), 215–219. <https://doi.org/10.1038/s41561-019-0298-6>
- Woodcock, N. H., Miller, A. V. M., & Woodhouse, C. D. (2014). Chaotic breccia zones on the Pembroke Peninsula, south Wales: Evidence for collapse into voids along dilational faults. *Journal of Structural Geology*, *69*, 91–107. <https://doi.org/10.1016/j.jsg.2014.09.019>
- Woodcock, N. H., Omma, J. E., & Dickson, J. A. D. (2006). Chaotic breccia along the dent fault, NW England: Implosion or collapse of a fault void? *Journal of the Geological Society*, *163*(3), 431–446. <https://doi.org/10.1144/0016-764905-067>
- Wu, L. Y., Hu, R. Z., Li, X. F., Stuart, F. M., Jiang, G. H., Qi, Y. Q., & Zhu, J. J. (2018). Mantle volatiles and heat contributions in high sulfidation epithermal deposit from the Zijinshan Cu–Au–Mo–Ag orefield, Fujian Province, China: Evidence from He and Ar isotopes. *Chemical Geology*, *480*, 58–65. <https://doi.org/10.1016/j.chemgeo.2017.08.005>
- Yan, J., Mavrogenes, J. A., Liu, S., & Coulson, I. M. (2020). Fluid properties and origins of the Lannigou Carlin-type gold deposit, SW China: Evidence from SHRIMP oxygen isotopes and LA-ICP-MS trace element compositions of hydrothermal quartz. *Journal of Geochemical Exploration*, *215*, 106546. <https://doi.org/10.1016/j.gexplo.2020.106546>



- Yeats, C. J., Hollis, S. P., Halfpenny, A., Corona, J. C., LaFlamme, C., Southam, G., et al. (2017). Actively forming Kuroko-type volcanic-hosted massive sulfide (VHMS) mineralization at Iheya North, Okinawa Trough, Japan. *Ore Geology Reviews*, *84*, 20–41. <https://doi.org/10.1016/j.oregeorev.2016.12.014>
- Ylagan, R. F., Altaner, S. P., & Pozzuoli, A. (1996). Hydrothermal alteration of a rhyolitic hyaloclastite from Ponza Island, Italy. *Journal of Volcanology and Geothermal Research*, *74*(3–4), 215–231. [https://doi.org/10.1016/s0377-0273\(96\)00046-7](https://doi.org/10.1016/s0377-0273(96)00046-7)
- Ylagan, R. F., Altaner, S. P., & Pozzuoli, A. (2000). Reaction mechanisms of smectite illitization associated with hydrothermal alteration from Ponza Island, Italy. *Clays and Clay Minerals*, *48*(6), 610–631. <https://doi.org/10.1346/ccmn.2000.0480603>
- Zitellini, N., Marani, M., & Borsetti, A. M. (1984). Post-orogenic tectonic evolution of Palmarola and Ventotene basins (Pontine Archipelago). *Memorie della Societa Geologica Italiana*, *27*, 121–131.

## References From the Supporting Information

- Atkinson, A. B., Jr. (2002). A model for the PTX properties of H<sub>2</sub>O–NaCl. (M. Sc. Thesis) Faculty of Virginia Polytechnic Institute and State University, USA.
- Bernasconi, S. M., Daëron, M., Bergmann, K. D., Bonifacie, M., Meckler, A. N., Affek, H. P., et al. (2021). InterCarb: A community effort to improve inter-laboratory standardization of the carbonate clumped isotope thermometer using carbonate standards. *Geochemistry, Geophysics, Geosystems*, *22*(5), e2020GC009588. <https://doi.org/10.1002/essoar.10504430.2>
- Bernasconi, S. M., Hu, B., Wacker, U., Fiebig, J., Breitenbach, S. F. M., & Rutz, T. (2013). Background effects on Faraday collectors in gas-source mass spectrometry and implications for clumped isotope measurements. *Rapid Communications in Mass Spectrometry*, *27*(5), 603–612. <https://doi.org/10.1002/rcm.6490>
- Bodnar, R., & Vityk, M. O. (1994). Interpretation of microthermometric data for H<sub>2</sub>O–NaCl fluid inclusions. In B. De Vivo, & M. L. Frezzotti (Eds.), *Fluid inclusions in minerals: Methods and applications* (pp. 117–130). Virginia Tech.
- Bodnar, R. J. (1983). A method of calculating fluid inclusion volumes based on vapor bubble diameters and PVTX properties of inclusion fluids. *Economic Geology*, *78*(3), 535–542. <https://doi.org/10.2113/gsecongeo.78.3.535>
- Bodnar, R. J. (1993). Revised equation and table for determining the freezing point depression of H<sub>2</sub>O–NaCl solutions. *Geochimica et Cosmochimica Acta*, *57*(3), 683–684. [https://doi.org/10.1016/0016-7037\(93\)90378-a](https://doi.org/10.1016/0016-7037(93)90378-a)
- Fernandez, A., Müller, I. A., Rodríguez-Sanz, L., van Dijk, J., Looser, N., & Bernasconi, S. M. (2017). A reassessment of the precision of carbonate clumped isotope measurements: Implications for calibrations and paleoclimate reconstructions. *Geochemistry, Geophysics, Geosystems*, *18*(12), 4375–4386. <https://doi.org/10.1002/2017gc007106>
- John, C. M., & Bowen, D. (2016). Community software for challenging isotope analysis: First applications of “Easotope” to clumped isotopes. *Rapid Communications in Mass Spectrometry*, *30*(21), 2285–2300. <https://doi.org/10.1002/rcm.7720>
- Lecumberri-Sanchez, P., Steele-MacInnis, M., & Bodnar, R. J. (2012). A numerical model to estimate trapping conditions of fluid inclusions that homogenize by halite disappearance. *Geochimica et Cosmochimica Acta*, *92*, 14–22. <https://doi.org/10.1016/j.gca.2012.05.044>
- Meckler, A. N., Ziegler, M., Millán, M. I., Breitenbach, S. F. M., & Bernasconi, S. M. (2014). Long-term performance of the Kiel carbonate device with a new correction scheme for clumped isotope measurements. *Rapid Communications in Mass Spectrometry*, *28*(15), 1705–1715. <https://doi.org/10.1002/rcm.6949>
- Müller, I. A., Fernandez, A., Radke, J., Van Dijk, J., Bowen, D., Schwieters, J., & Bernasconi, S. M. (2017). Carbonate clumped isotope analyses with the long-integration dual-inlet (LIDI) workflow: Scratching at the lower sample weight boundaries. *Rapid Communications in Mass Spectrometry*, *2*(12), 1057–1066. <https://doi.org/10.1002/rcm.7878>
- Müller, I. A., Rodríguez-Blanco, J. D., Storck, J. C., do Nascimento, G. S., Bontognali, T. R., Vasconcelos, C., et al. (2019). Calibration of the oxygen and clumped isotope thermometers for (proto-)dolomite based on synthetic and natural carbonates. *Chemical Geology*, *525*, 1–17. <https://doi.org/10.1016/j.chemgeo.2019.07.014>
- Rizzo, A. L., Barberi, F., Carapezza, M. L., Di Piazza, A., Francalanci, L., Sortino, F., & D'Alessandro, W. (2015). New mafic magma refilling a quiescent volcano: Evidence from He–Ne–Ar isotopes during the 2011–2012 unrest at Santorini, Greece. *Geochemistry, Geophysics, Geosystems*, *16*(3), 798–814. <https://doi.org/10.1002/2014gc005653>
- Rizzo, A. L., Pelorosso, B., Coltorti, M., Ntaflos, T., Bonadiman, C., Matusiak-Malek, M., et al. (2018). Geochemistry of Noble gases and CO<sub>2</sub> in fluid Inclusions from Lithospheric mantle beneath Wilcza Góra (Lower Silesia, Southwest Poland). *Frontiers of Earth Science*, *6*, 215. <https://doi.org/10.3389/feart.2018.00215>
- Robidoux, P., Aiuppa, A., Rotolo, S. G., Rizzo, A. L., Hauri, E. H., & Frezzotti, M. L. (2017). Volatile contents of mafic-to-intermediate magmas at San Cristóbal volcano in Nicaragua. *Lithos*, *272*, 147–163. <https://doi.org/10.1016/j.lithos.2016.12.002>
- Sano, Y., Urabe, A., Wakita, H., Chiba, H., & Sakai, H. (1985). Chemical and isotopic compositions of gases in geothermal fluids in Iceland. *Geochemical Journal*, *19*(3), 135–148. <https://doi.org/10.2343/geochemj.19.135>
- Schmid, T. W., & Bernasconi, S. M. (2010). An automated method for “clumped-isotope” measurements on small carbonate samples. *Rapid Communications in Mass Spectrometry*, *24*(14), 1955–1963. <https://doi.org/10.1002/rcm.4598>
- Sharp, Z. D. (1990). A laser-based microanalytical method for the in situ determination of oxygen isotope ratios of silicates and oxides. *Geochimica et Cosmochimica Acta*, *54*(5), 1353–1357. [https://doi.org/10.1016/0016-7037\(90\)90160-m](https://doi.org/10.1016/0016-7037(90)90160-m)
- Steele-MacInnis, M., Bodnar, R. J., & Naden, J. (2011). Numerical model to determine the composition of H<sub>2</sub>O–NaCl–CaCl<sub>2</sub> fluid inclusions based on microthermometric and microanalytical data. *Geochimica et Cosmochimica Acta*, *75*(1), 21–40. <https://doi.org/10.1016/j.gca.2010.10.002>
- Steele-MacInnis, M., Lecumberri-Sanchez, P., & Bodnar, R. J. (2012). Short note: HokieFlincs\_H<sub>2</sub>O–NaCl: A Microsoft Excel spreadsheet for interpreting microthermometric data from fluid inclusions based on the PVTX properties of H<sub>2</sub>O–NaCl. *Computers & Geosciences*, *49*, 334–337. <https://doi.org/10.1016/j.cageo.2012.01.022>
- Stern, S. M., Hall, D. L., & Bodnar, R. J. (1988). Synthetic fluid inclusions. V. Solubility relations in the system NaCl–KCl–H<sub>2</sub>O under vapor-saturated conditions. *Geochimica et Cosmochimica Acta*, *52*(5), 989–1005. [https://doi.org/10.1016/0016-7037\(88\)90254-2](https://doi.org/10.1016/0016-7037(88)90254-2)